A TURNING-BAND METHOD FOR THE SIMULATION OF ANISOTROPIC FRACTIONAL BROWNIAN FIELDS.

HERMINE BIERMÉ [1,2], LIONEL MOISAN [1], AND FRÉDÉRIC RICHARD[3]

ABSTRACT. In this paper, we propose a method for simulating realizations of two-dimensional anisotropic fractional Brownian fields (AFBF) introduced by Bonami and Estrade (2003). The method is adapted from a generic simulation method called the turning-band method (TBM) due to Matheron (1973). The TBM reduces the problem of simulating a field in two dimensions by combining independent processes simulated on oriented bands. In the AFBF context, the simulation fields are constructed by solving an integral equation arising from the application of the TBM to non-stationary anisotropic fields. This garantees the convergence of simulations as their precision is increased. The construction is followed by a theoretical study of the convergence rate. Another key feature of this work is the simulation of band processes. Using self-similarity properties, processes are simulated exactly on bands with a circulant embedding method, so that simulation errors are exclusively due to the field approximation. Moreover, we design a Dynamic Programming algorithm that selects band orientations achieving the optimal trade-off between computational cost and precision. Finally, we conduct a numerical study showing that the approximation error does not significantly depend on the regularity of the fields to be simulated, nor on their degree of anisotropy. Experiments also suggest that simulations preserve field statistical properties.

1. INTRODUCTION

In this paper, we address the issue of simulating realizations of a generic class of Gaussian fields, known as Anisotropic Fractional Brownian Fields (AFBF) and introduced in [9].

These fields represent anisotropic extensions of usual fractional Brownian fields (FBF), which are themselves isotropic extensions in several dimensions of the famous fractional Brownian motion (FBM) [26, 29]. Having stationary increments, they are characterized by a variogram v (see Equation (6) later) satisfying the relation

$$(1) \qquad \forall\, x \in \mathbb{R}^2, \quad v(x) = \frac{1}{2} \int_{\mathbb{R}^2} \left| e^{ix \cdot \zeta} - 1 \right|^2 f(\zeta) d\zeta$$

for a spectral density of the form

$$(2) \qquad \forall\, \zeta \in \mathbb{R}^2, \quad f(\zeta) = c(\arg(\zeta)) \|\zeta\|^{-2h(\arg(\zeta))-2},$$

where $\|\zeta\|$ is the Euclidean norm of ζ, $\arg(\zeta)$ is the direction of ζ, and $x \cdot \zeta$ denotes the canonical inner product on $\mathbb{R}^2$. Functions c and h are two π-periodic mesurable functions, identified with functions defined on $(-\pi/2, \pi/2]$, with ranges satisfying $c((-\pi/2, \pi/2]) \subset \mathbb{R}^+$ and $h((-\pi/2, \pi/2]) \subset (0, 1)$. When functions c and h are both constant ($c \equiv C > 0$ and $h \equiv H$), the obtained field corresponds to a FBF of order H.

The simulation of AFBF is an open issue whose complexity is mainly due to both the non-stationarity and the anisotropy of the fields. In [41], Stein described a specific method for the simulation of (isotropic) FBF. This method is based on a representation of the FBF by a locally stationary isotropic Gaussian field, which is simulated using circulant embedding matrix techniques developped in [42]. This simulation is exact and efficient on a regular grid. However, no locally stationary representation is available for general anisotropic fields so that Stein's method cannot be extended to this situation. More generic methods based on covariance matrix factorizations [11, 12] can theoretically be applied to the AFBF simulation issue, but their computational cost is prohibitive and covariance functions are not known explicitly in the general case. Other methods based on the discretization of a continous spectral representation of the field were used for the simulation of FBF in [38] and AFBF in [3, 7]. However, due to truncation or periodization of the spectral representation, the statistical properties of the simulated field does not exactly match those of the theoretical field.

In this paper, we focus on another generic simulation method, called the turning-band method (TBM) [25, 32]. The TBM essentially reduces the problem of simulating a field in several dimensions to the problem of simulating several processes in one dimension. Indeed, consider the problem of generating a realization of a target field X on a discrete set G of points of $\mathbb{R}^2$. Choose n lines (called turning bands) passing through a given origin and denote by θ_i the angle indicating the direction of the ith band. The TBM is based on a combination of n appropriate processes $(Y_i)_{1 \leq i \leq n}$ independently simulated on each predefined band:

$$(3) \qquad \forall\, x \in G, \quad X_n(x) = \sum_{i=1}^{n} \sqrt{\lambda_i}\, Y_i(x \cdot u(\theta_i)),$$

where the λ_i's are positive weights and $u(\theta) = (\cos(\theta), \sin(\theta))$ is the unit vector with direction θ. There are two major issues raised by the TBM. The first one consists of determining appropriate weights λ_i and band processes Y_i which ensure the convergence of the turning-band field X_n to the target field X as n tends to infinity. The second one concerns the simulation of the processes Y_i on the non-equispaced points $\{x \cdot u(\theta_i), x \in G\}$.

The convergence issue has been extensively studied in the case when the target field is stationary [10, 15, 17, 23, 24, 30, 32]. In this case, the convergence can be obtained using stationary band processes. Let $\tilde{C}_\theta$ be the covariance of a band process in the direction θ. Take orientations $(\theta_i)_{1 \leq i \leq n}$ uniformly distributed over $(-\pi/2, \pi/2)$, and set $\lambda_i = \frac{\pi}{n}$. Then, the covariance of X_n at point x is $C_n(x) = \frac{\pi}{n} \sum_{i=1}^{n} \tilde{C}_{\theta_i}(x \cdot u(\theta_i))$ and, as a Riemann sum, it converges to $T(\tilde{C})(x) = \int_{-\frac{\pi}{2}}^{\frac{\pi}{2}} \tilde{C}_\theta(x \cdot u(\theta)) d\theta$ as n tends to infinity. Hence, for the turning-band field X_n to converge to a target field X of covariance C_X, it suffices that $\tilde{C}$ satisfies the condition $T(\tilde{C}) \equiv C_X$. In the special case when the target field is isotropic, $\tilde{C}_\theta \equiv \tilde{C}_0$ does not depend on θ, and the previous condition reduces to $T(C_0) \equiv C_X$. This integral equation was solved explicitly for many different types of covariance C_X (Gaussian, Whittle-Matérn, Cauchy, etc.), making possible to apply the TBM to a wide range of stationary isotropic fields [10, 15, 17, 23, 24, 28]. In the anisotropic case, the

equation was solved from spectral representations of covariances by expressing spectral densities of processes as a function of the one of the target field [30].

The TBM can also be adapted to the simulation of non-stationnary fields with stationary increments. In such a situation, the convergence of the turning-band field to the target one is rather expressed in terms of variograms. It can be obtained by taking band processes with stationary increments and variograms $\tilde{v}_\theta$ (in the direction θ) which satisfy the condition

$$(4) \qquad v_X(x) = \int_{-\frac{\pi}{2}}^{\frac{\pi}{2}} \tilde{v}_\theta(y \cdot u(\theta)) d\theta,$$

where v_X is the variogram of the target field (see Equation (6) later). In [45], the previous integral equation was solved in the particular case when v_X is the variogram of an (isotropic) FBF of order H. It was shown that variograms v_θ do not depend on θ and are proportional to the variogram of a one-dimensional FBM of the same order H. In [20], this result was extended to other non-stationary isotropic Gaussian fields with spline generalized covariance. Similar ideas can be found in [19, 31, 34] about the simulation of the so-called intrinsic random fields of order k generalizing fields with stationary increments [13, 32]. However, none of these works directly addressed the issue of simulating non-stationary anisotropic fields. In [39, 43], some attempts were made for the simulation of such fields with a TBM, but they only cover a few special cases. Let us also emphasize that the simulated fields are not Gaussian, so that Gaussian realizations may only be approximated by averaging several independent realizations and applying a Central Limit Theorem.

One of the main originalities of this paper is the construction of appropriate turning-band fields for the simulation of AFBF, which are themselves centered Gaussian random fields with stationary increments. This is done by solving Equation (4) when v_X is defined by Equations (1) and (2). This construction is completed by an analysis of the simulation error from both theoretical and numerical viewpoints. This study brings new insights into

the TBM simulation error, which had been mainly investigated in the stationary isotropic case [14, 24, 31].

In the construction of turning-band fields for AFBF, we show that band processes are one dimensional FBMs with varying Hurst indices. Hence, the application of the TBM to AFBF directly leads to the issue of simulating these processes on non-uniformly spaced points. In the context of TBM application, Yin [45] simulated FBMs using an adaptation of the spectral method [31, 33, 40]. Based on a discretization of the spectral density of the process covariance, this method induces periodization effects and is inaccurate for mainly two reasons: the simulated process is not Gaussian and its covariance function only approximates the target one. In [20, 21], periodization effects induced by Fourier methods was overcome using a continous spectral method. This method is fast and can be applied with arbitrary simulation points. However, it does not produce Gaussian realizations neither. In another context, Perrin *et al.* [35] developed a circulant embedding method (see [18, 42] and Section 3.1) for the simulation of FBF. This method is fast and exact but requires equispaced simulation points. However, as shown in this paper, the issue of simulating FBM on band points can be reexpressed on equispaced points using self-similarity properties of FBM, as soon as bands orientations are conveniently chosen. Hence, we can apply the circulant embedding method to obtain exact simulations of FBM on band points but the cost of these simulations depends on band orientations, and is higher than the one of the continuous spectral method in [20, 21]. To reduce the global computational cost, we thus propose a Dynamic Programming [4] algorithm that selects band orientations in an optimal way.

2. Turning-band method

2.1. **Anisotropic fractional Brownian fields.** Let $(\Omega, \mathcal{A}, \mathbb{P})$ be a probability space. A 2-dimensional random field X is a map from $\Omega \times \mathbb{R}^2$ into $\mathbb{R}$ such that $X(\cdot, y) := X(y)$ is a real random variable on Ω for all $y \in \mathbb{R}^2$. A random field is Gaussian if any finite linear combination of its associated random variables is a Gaussian variable. A centered

Gaussian field X is characterized by its covariance function: $(y, z) \mapsto \text{Cov}(X(y), X(z))$. A field X has stationary increments if the law governing the field $X(\cdot + z) - X(z)$ is the same as $X(\cdot) - X(0)$ for all $z \in \mathbb{R}^d$.

When the field X is centered and with stationary increments, we have

$$(5) \qquad \forall y, z \in \mathbb{R}^2, \quad \text{Cov}(X(y), X(z)) = v_X(y) + v_X(z) - v_X(y - z),$$

where v_X is the so-called variogram of X defined as

$$(6) \qquad \forall y \in \mathbb{R}^2, \quad v_X(y) = \frac{1}{2}\mathbb{E}((X(y) - X(0))^2).$$

Hence, if the field X is also Gaussian, its law is characterized by its variogram (6).

In this work, we deal with anisotropic fractional Brownian fields, which are centered Gaussian fields with stationary increments, characterized by a variogram of the form (1) with a spectral density defined as in Equation (2). When $c \equiv C > 0$ and $h \equiv H \in (0, 1)$ are both constant, the variogram satisfies (see Remark 1.1.13 of [27] for instance)

$$(7) \qquad v(x) = \frac{1}{2}\int_{\mathbb{R}^2}\left|e^{ix\cdot\zeta} - 1\right|^2 C\|\zeta\|^{-2H-d}d\xi = C\frac{\pi^{\frac{1}{2}}\Gamma(H + 1/2)\gamma(H)}{2\Gamma(H + 1)}\|x\|^{2H},$$

where for all $H \in (0, 1)$,

$$(8) \qquad \gamma(H) = \frac{\pi}{H\Gamma(2H)\sin(H\pi)}.$$

It follows that such fields are isotropic, which means that their law is invariant under rotation. They are also H-self-similar. When the function c is not constant but $h \equiv H$ remains constant, the field remains self-similar of order H but becomes anisotropic. When h is also allowed to vary, the field is not self-similar anymore but, setting $H = \operatorname*{essinf}_{\theta \in S^{d-1}; c(\theta) > 0} h(\theta)$, one can still find a continuous modification of X with H as critical Hölder exponent [9]. The fractal dimension of its graph is still linked with H by the relation $D = 2 - H$ a.s. (see [44] for instance).

In general, it is difficult to get an explicit form of the AFBF variogram similar to the one expressed for the FBF in Equation (7). However, we have computed explicitely the variogram of a particular class of AFBF which is slightly more general than the FBF.

This field, that we call elementary field, is defined by a spectral density of the form (2) with $c = \mathbf{1}_{[\alpha_1,\alpha_2]}$ for $-\pi/2 \leq \alpha_1 < \alpha_2 \leq \pi/2$, and $h \equiv H$ for $H \in (0,1)$. When $\alpha_2 = -\alpha_1 = \pi/2$, an elementary field corresponds to a FBF of order H. As explained in Section 4, elementary fields will be of particular interest for the numerical evaluation of simulations.

Proposition 2.1. *Let $H \in (0,1)$ and $-\pi/2 \leq \alpha_1 < \alpha_2 \leq \pi/2$. Let denote v_{H,α_1,α_2} the variogram of an AFBF with $h = H$ and $c = \mathbf{1}_{[\alpha_1,\alpha_2]}$. Then,*

$$(9) \qquad \forall x \in \mathbb{R}^2, \; v_{H,\alpha_1,\alpha_2}(x) = 2^{2H-1}\gamma(H)C_{H,\alpha_1,\alpha_2}(\arg(x))\|x\|^{2H},$$

where $\|x\|$ is the Euclidean norm of x and C_{H,α_1,α_2} is a π-periodic function defined on $(-\pi/2,\pi/2]$ by

$$C_{H,\alpha_1,\alpha_2}(\theta) = \begin{cases} \beta_H\left(\frac{1-\sin(\alpha_2-\theta)}{2}\right) + \beta_H\left(\frac{1-\sin(\alpha_1-\theta)}{2}\right) & if \quad \alpha_1 \leq \theta + \pi/2 \leq \alpha_2 \\ \beta_H\left(\frac{1+\sin(\alpha_2-\theta)}{2}\right) + \beta_H\left(\frac{1+\sin(\alpha_1-\theta)}{2}\right) & if \quad \alpha_1 \leq \theta - \pi/2 \leq \alpha_2 \\ \left|\beta_H\left(\frac{1-\sin(\alpha_2-\theta)}{2}\right) - \beta_H\left(\frac{1-\sin(\alpha_1-\theta)}{2}\right)\right| & otherwise \end{cases}$$

with β_H the Beta incomplete function given by

$$\forall t \in [0,1], \; \beta_H(t) = \int_0^t u^{H-1/2}(1-u)^{H-1/2}du,$$

and $\gamma(H)$ is defined in Equation (8).

The proof of this proposition is given in appendix A. Now, let us consider the general case from which the TBM will follow.

2.2. **Turning-band fields for AFBF.**
By a change of variables in polar coordinates, we derive an integral expression for the variogram of an AFBF.

Proposition 2.2. *Let X be a centered Gaussian field with stationary increments. Let us assume that its variogram v_X is of the form (1) with a spectral density defined by (2) with c and h two π-periodic mesurable functions with ranges satisfying $c((-\pi/2,\pi/2]) \subset \mathbb{R}^+$*

and $h((-\pi/2, \pi/2]) \subset (0, 1)$. Then, for all $x \in \mathbb{R}^2$

$$(10) \qquad v_X(x) = \frac{1}{2} \int_{-\pi/2}^{\pi/2} \gamma(h(\theta)) c(\theta) |x \cdot u(\theta)|^{2h(\theta)} d\theta,$$

where $u(\theta) = (\cos(\theta), \sin(\theta))$ and $\gamma(H)$ is defined in Equation (8).

Proof. Let $x \in \mathbb{R}^2$. Then acording to (1) and (2),

$$\begin{aligned} 2v_X(x) &= \int_{\mathbb{R}^2} \left| e^{ix \cdot \zeta} - 1 \right|^2 c(\arg(\zeta)) |\zeta|^{-2h(\arg(\zeta)) - 2} d\zeta \\ &= \int_0^{2\pi} \int_0^{+\infty} \left| e^{ir(x \cdot u(\theta))} - 1 \right|^2 c(\theta) r^{-2h(\theta) - 1} dr d\theta, \end{aligned}$$

by a change of variables in polar coordinates. But, for $H \in (0, 1)$ and $t \in \mathbb{R}$,

$$\int_0^{+\infty} \left| e^{irt} - 1 \right|^2 r^{-2H-1} dr = \frac{1}{2} \int_{\mathbb{R}} \left| e^{ist} - 1 \right|^2 |s|^{-2H-1} ds = \frac{1}{2} \gamma(H) |t|^{2H},$$

according to (7.2.13) of [37]. Then the result follows by π-periodicity of h and c. □

The integral equation (10) is of the form (4) with $\tilde{v}_\theta(\cdot) = \gamma(h(\theta)) c(\theta) \frac{1}{2} |\cdot|^{2h(\theta)}$. This means that $\tilde{v}_\theta$ is a solution of the integral equation (4) when v_X is the variogram of an AFBF. Now recall that a FBM of order H is a centered Gaussian process with stationary increments and variogram $w_H(t) = \frac{1}{2} |t|^{2H}$ for all $t \in \mathbb{R}$. Hence, ignoring the factor $\gamma(h(\theta)) c(\theta)$ depending on the orientation θ, the variogram $\tilde{v}_\theta$ is equal to the one of a FBM of order $h(\theta)$, also varying with θ.

According to previous remarks, we now specify turning-band fields for AFBF simulations. Given an ordered set $\Theta = (\theta_i)_{1 \leq i \leq n}$ of band orientations $-\pi/2 \leq \theta_1 < \ldots < \theta_n \leq \pi/2$, and a set $\Lambda = (\lambda_i)_{1 \leq i \leq n} \in [0, +\infty)^n$ of appropriate band weights, turning-band fields have the form

$$(11) \qquad X_{\Theta, \Lambda}(x) = \sum_{i=1}^n \sqrt{\lambda_i \gamma(h(\theta_i)) c(\theta_i)} Y_i(x \cdot u(\theta_i)), \ \forall x \in \mathbb{R}^2,$$

where the Y_i's are n independent FBM of order $h(\theta_i)$. In the remaining of the text, turning-band fields $X_{\Theta, \Lambda}$ will be called the simulation fields and processes Y_i will always

be FBF of order $h(\theta_i)$. We will also describe the precision of simulation fields $X_{\Theta,\Lambda}$ using the variable

$$(12) \qquad \varepsilon_\Theta = \max_{i=1,\cdots,n+1} (\theta_i - \theta_{i-1}), \quad \text{with } n = |\Theta|,$$

and $\theta_0 \in [-\pi/2, \theta_1]$ and $\theta_{n+1} \in [\theta_n, \pi/2]$ are fixed directions chosen according to the AFBF function c. Remark that a uniform choice for the orientations consists in choosing $\theta_n = \theta_{n+1} = \pi/2$ and $\theta_i = -\pi/2 + i\pi/n$ for $0 \le i \le n$. This choice leads to $\varepsilon_\Theta = \frac{\pi}{n}$ while, for general orientations, we always have $\varepsilon_\Theta \ge \frac{\theta_n - \theta_0}{n} \ge \frac{\theta_n - \theta_1}{n}$.

The error of simulating X by $X_{\Theta,\Lambda}$ may be expressed, at point $x \in \mathbb{R}^2$, as the Kolmogorov distance between the random variables $X_{\Theta,\Lambda}(x)$ and $X(x)$, that is,

$$(13) \qquad d_{Kol}(X_{\Theta,\Lambda}(x), X(x)) = \sup_{t \in \mathbb{R}} |\mathbb{P}(X_{\Theta,\Lambda}(x) \le t) - \mathbb{P}(X(x) \le t)|.$$

When this distance tends to 0, it implies that the random variable $X_{\Theta,\Lambda}(x)$ tends to $X(x)$ in distribution. As stated next, due to our Gaussian framework, this distance can be further bounded by a distance between variograms of simulation and target fields at x.

Theorem 2.3. *Let $X_{\Theta,\Lambda}$ be a simulation field defined as in Equation (11). Then, $X_{\Theta,\Lambda}$ is a centered Gaussian random field on $\mathbb{R}^2$ with stationary increments and variogram*

$$(14) \qquad v_{\Theta,\Lambda}(x) := \sum_{i=1}^{n} \lambda_i \gamma(h(\theta_i)) c(\theta_i) w_{h(\theta_i)}(x \cdot u(\theta_i)).$$

Moreover, $X_{\Theta,\Lambda}(0) = X(0) = 0$ a.s. and, for all $x \ne 0$,

$$(15) \qquad d_{Kol}(X_{\Theta,\Lambda}(x), X(x)) \le 2\frac{|v_X(x) - v_{\Theta,\Lambda}(x)|}{v_X(x)}.$$

Choosing $(\Theta_n, \Lambda_n)_n$ in such a way that $v_{\Theta_n,\Lambda_n}(x) \underset{n\to+\infty}{\longrightarrow} v_X(x)$ for all $x \in \mathbb{R}^2$,

$$(X_{\Theta_n,\Lambda_n}(x))_{x\in\mathbb{R}^2} \xrightarrow[n\to+\infty]{fdd} (X(x))_{x\in\mathbb{R}^2},$$

where $\xrightarrow{fdd}$ stands for convergence of finite dimensional distributions.

Proof. Let us write $X_{\theta_i}(x) := Y_i(x \cdot u(\theta_i))$, for $x \in \mathbb{R}^2$, with Y_i a FBM of order $h(\theta_i)$. First, remark that $X_{\theta_i}(0) = Y_i(0) = 0$ a.s. Moreover, since Y_i is a centered Gaussian random

process it is clear that X_{θ_i} is a centered Gaussian random field on $\mathbb{R}^2$. Finally, since Y_i has stationary increments, for any $x_0 \in \mathbb{R}^2$, writing $t_{0,i} = x_0 \cdot u(\theta_i) \in \mathbb{R}$,

$$
\begin{aligned}
\{X_{\theta_i}(x + x_0) - X_{\theta_i}(x_0); x \in \mathbb{R}^2\} &= \{Y_i(x \cdot u(\theta_i) + t_{0,i}) - Y_i(t_{0,i}); x \in \mathbb{R}^2\} \\
&\stackrel{fdd}{=} \{Y_i(x \cdot u(\theta_i)) - Y_i(0); x \in \mathbb{R}^2\}, \\
&= \{X_{\theta_i}(x) - X_{\theta_i}(0); x \in \mathbb{R}^2\}.
\end{aligned}
$$

It follows that $X_{\Theta,\Lambda}$ is a centered Gaussian random field on $\mathbb{R}^2$ with stationary increments as a sum of independent centered Gaussian random fields on $\mathbb{R}^2$ with stationary increments fields. Since $X_{\Theta,\Lambda}(0) = 0$ a.s.,

$$
\begin{aligned}
v_{X_{\Theta,\Lambda}}(x) &= \frac{1}{2}\mathbb{E}\left(X_{\Theta,\Lambda}(x)^2\right) = \frac{1}{2}\mathrm{Var}(X_{\Theta,\Lambda}(x)), \text{ since } X_{\Theta,\Lambda} \text{ is centered,} \\
&= \frac{1}{2}\sum_{i=1}^n \lambda_i \gamma(h(\theta_i))c(\theta_i)\mathrm{Var}(Y_i(x \cdot u(\theta_i))), \text{ by independence,} \\
&= \frac{1}{2}\sum_{i=1}^n \lambda_i \gamma(h(\theta_i))c(\theta_i)|x \cdot u(\theta_i)|^{2h(\theta_i)} = v_{\Theta,\Lambda}(x).
\end{aligned}
$$

Let $N \sim \mathcal{N}(0,1)$, then for $x \neq 0$,

$$
d_{Kol}(X_{\Theta,\Lambda}(x), X(x)) = d_{Kol}(\sqrt{v_{\Theta,\Lambda}(x)}N, \sqrt{v_X(x)}N).
$$

Then (15) follows from the fact that $d_{Kol}(\sigma'N, \sigma N) \leq 2\frac{|\sigma - \sigma'|}{\sigma}$, already remarked in [6]. Actually, there is nothing to prove when $\frac{|\sigma - \sigma'|}{\sigma} > \frac{1}{2}$. Otherwise we use the fact that for $\sigma > 1$ and $z > 0$ one has $\mathbb{P}(z < N \leq \sigma z) \leq (\sigma - 1)ze^{-z^2/2} \leq \sigma^2 - 1$.

Now, let assume that (Θ_n, Λ_n) is such that $v_{\Theta_n,\Lambda_n}(x) \underset{n \to +\infty}{\longrightarrow} v_X(x)$ for all $x \in \mathbb{R}^2$. By stationarity of the increments, for all $n \geq 1$, for all $x, y \in \mathbb{R}^2$,

$$
\mathrm{Cov}(X_{\Theta_n,\Lambda_n}(x), X_{\Theta_n,\Lambda_n}(y)) = v_{\Theta_n,\Lambda_n}(x) + v_{\Theta_n,\Lambda_n}(y) - v_{\Theta_n,\Lambda_n}(x - y),
$$

and similarly for $\mathrm{Cov}(X(x), X(y))$ and v_X. It follows that $\mathrm{Cov}(X_{\Theta_n,\Lambda_n}(x), X_{\Theta_n,\Lambda_n}(y))$ tends to $\mathrm{Cov}(X(x), X(y))$ for all $x, y \in \mathbb{R}^2$. Using a Cramér-Wold device, this implies that the field $(X_{\Theta_n,\Lambda_n}(x))_{x \in \mathbb{R}^2}$ converges to $(X(x))_{x \in \mathbb{R}^2}$, for finite dimensional distributions. $\quad\square$

Let us quote that, since $v_{\Theta,\Lambda}$ appears as a numerical approximation of the integral giving v_X, one can choose $(\Theta_n, \Lambda_n)_n$ in such a way that $v_{\Theta_n,\Lambda_n}(x)$ tends to $v(x)$ for $x \in \mathbb{R}^2$. This implies that $d_{Kol}(X_{\Theta_n,\Lambda_n}(x), X(x)) \to 0$ so that $X_{\Theta_n,\Lambda_n}(x)$ tends to $X(x)$ in distribution. Note that conversely, since $X_{\Theta_n,\Lambda_n}(x)$ and $X(x)$ are centered Gaussian variables, $v_{\Theta_n,\Lambda_n}(x)$ tends to $v(x)$ as soon as $X_{\Theta_n,\Lambda_n}(x)$ tends to $X(x)$ in distribution. The next section is devoted to the rate of convergence.

2.3. Approximation error.
We can choose Θ, Λ such that the following uniform bounds hold for approximation of elementary fields.

Proposition 2.4. *Let c and h be two π-periodic mesurable functions defined on $(-\pi/2, \pi/2]$ by $h = H$ for some $H \in (0,1)$ and $c = \mathbf{1}_{[\alpha_1,\alpha_2]}$ for $-\pi/2 \leq \alpha_1 < \alpha_2 \leq \pi/2$. Let $\Theta = (\theta_i)_{1 \leq i \leq n}$ with $\alpha_1 \leq \theta_1 < \ldots < \theta_n \leq \alpha_2$ and $\theta_0 = \alpha_1$, $\theta_{n+1} = \alpha_2$. Choose Λ as*

$$(16) \qquad \lambda_1 = \theta_2 - \theta_0 \text{ and } \lambda_i = \theta_{i+1} - \theta_i \text{ for } 2 \leq i \leq n.$$

Then, one can find a positive constant $C > 0$, independent of Θ, Λ, such that for all $x \in \mathbb{R}^d$,

$$(17) \qquad d_{Kol}(X_{\Theta,\Lambda}(x), X_{H,\alpha_1,\alpha_2}(x)) \leq C\varepsilon_{\Theta}^{\min(2H,1)},$$

where the precision parameter ε_{Θ} is defined in Equation (12).
Moreover, when choosing

$$(18)$$
$$\lambda_1 = (\theta_1 - \theta_0) + \frac{\theta_2 - \theta_1}{2}, \ \lambda_n = (\theta_{n+1} - \theta_n) + \frac{\theta_n - \theta_{n-1}}{2} \text{ and } \lambda_i = \frac{\theta_{i+1} - \theta_{i-1}}{2} \text{ for } 2 \leq i \leq n-1,$$

one can find a positive constant $C > 0$, independent of Θ, Λ, such that for all $x \in \mathbb{R}^d$,

$$(19) \quad d_{Kol}(X_{\Theta,\Lambda}(x), X_{H,\alpha_1,\alpha_2}(x)) \leq C \begin{cases} \left(\varepsilon_{\Theta}^3 \delta_{\Theta}^{-2+\min(2H,1)} + \varepsilon_{\Theta}^{1+\min(2H,1)} \right) & \text{if } H \neq 1/2, \\ \left(\varepsilon_{\Theta}^3 \delta_{\Theta}^{-1} |\log(\delta_{\Theta})| + \varepsilon_{\Theta}^2 \right) & \text{if } H = 1/2 \end{cases}$$

with $\delta_{\Theta} = \min\limits_{1 \leq i \leq n-1} (\theta_{i+1} - \theta_i)$.

The proof of Proposition 2.4 is postponed to Appendix B. In [22], the authors also propose a TBM to synthesize isotropic FBF (case $\alpha_1 = -\pi/2$ and $\alpha_2 = \pi/2$) in general dimension $d \geq 2$. However, the processes simulated on the bands are not Gaussian so that the Kolmogorov distance between the simulated random variable and $X_{H,-\pi/2,\pi/2}(x)$ is bounded by the Berry Esseen bound given by $n^{-1/2}$, with n the number of bands, (see Equation (27) in [22]). Moreover, in their case this distance also depends on the point $x \in \mathbb{R}^2$. Let us compare with our results. Note that when orientations are chosen uniformly one has $\varepsilon_\Theta = \delta_\Theta = \frac{\alpha_2 - \alpha_1}{n}$ so that, choosing a rectangular rule, we obtain in (17) a bound given by $n^{-\min(2H,1)}$, while for a trapezoidal rule, we obtain in (19) a bound given by $n^{-1-\min(2H,1)}$ when $H \neq 1/2$ and $n^{-2}\log(n)$ when $H = 1/2$. Moreover let us emphasize that our bounds do not depend on $x \in \mathbb{R}^2$. This could be generalized to other self-similar AFBF ($h \equiv H$) under regularity assumptions on c. In the general case, our bounds depend on x through the term $1/v_X(x)$. However, we obtain uniform bounds for the difference $|v_X(x) - v_{\Theta,\Lambda}(x)|$ when x is in a compact set, as stated in the next proposition.

Proposition 2.5. *Let assume that h and c are piecewise $\mathcal{C}^1$ on $(-\pi/2, \pi/2]$. Let $\Theta = (\theta_i)_{1 \leq i \leq n}$ with $-\pi/2 \leq \theta_1 < \ldots < \theta_n \leq \pi/2$ containing the singular points of h and c and $\theta_0 = -\pi/2$, $\theta_{n+1} = \pi/2$. Let T be a compact set of $\mathbb{R}^d$. Then, one can find $\Lambda = (\lambda_i)_{1 \leq i \leq n} \in [0, +\infty)^n$ and a positive constant $C_T > 0$, independent of Θ, Λ, such that for all $x \in T$,*

$$(20) \qquad |v_X(x) - v_{\Theta,\Lambda}(x)| \leq C_T \varepsilon_\Theta^{\min(2H,1)},$$

where $H = \min\limits_{\theta \in [-\pi/2,\pi/2]} h(\theta) > 0$ and ε_Θ is defined in Equation (12). If moreover, h and c are piecewise $\mathcal{C}^2$ on $(-\pi/2, \pi/2]$, one can find $\Lambda = (\lambda_i)_{1 \leq i \leq n} \in [0, +\infty)^n$ and a positive constant $C_T > 0$, independent of Θ, Λ, such that for all $x \in T$,

$$(21) \qquad |v_X(x) - v_{\Theta,\Lambda}(x)| \leq C_T \begin{cases} \left(\varepsilon_\Theta^3 \delta_\Theta^{-2+\min(2H,1)} + \varepsilon_\Theta^{1+\min(2H,1)} \right) & \text{if } H \neq 1/2, \\ \left(\varepsilon_\Theta^3 \delta_\Theta^{-1} |\log(\delta_\Theta)| + \varepsilon_\Theta^2 \right) & \text{if } H = 1/2 \end{cases}$$

with $\delta_\Theta = \min_{1 \le i \le n-1} (\theta_{i+1} - \theta_i)$.

The proof of Proposition 2.5 is postponed to Appendix B. A bound for the Kolmogorov distance is then obtained using the fact that $d_{Kol}(X_{\Theta,\Lambda}(x), X(x)) \le 2 \frac{|v_X(x) - v_{\Theta,\Lambda}(x)|}{v_X(x)}$. Then we may choose an increasing sequence of $(\Theta_n)_n$ and choose $(\Lambda_n)_n$ as given in Proposition 2.5. Therefore, if $\varepsilon_{\Theta_n} \to 0$, the sequence of random fields $(X_{\Theta_n,\Lambda_n}(x))_{x \in \mathbb{R}^2}$ converges to $(X(x))_{x \in \mathbb{R}^2}$, for finite dimensional distributions in view of Theorem 2.3. The next section is devoted to the simulation of the band processes.

3. Fast and exact simulation on bands

3.1. **Simulation of 1D fractional Brownian motions.** Several methods for the synthesis of 1D fractional Brownian motions have been proposed in the literature. Most of them are approximate procedures. However, considering equispaced points on the band one can get exact simulations using the circulant embedding method [18]. Let us briefly recall this procedure. Let $H \in (0, 1)$ and B_H a fractional Brownian motion. We consider $Z_H = (B_H(t+1) - B_H(t))_{t \in \mathbb{R}}$, the fractional Gaussian noise that is a stationary process with covariance function given by

$$\text{Cov}(Z_H(t), Z_H(s)) = r_H(|t - s|) \text{ with } r_H(t) = \frac{1}{2}(|t+1|^{2H} - 2|t|^{2H} + |t-1|^{2H}).$$

Let $l \ge 1$, then the vector $(Z_H(0), \ldots, Z_H(l-1))$ is a centered Gaussian vector of size l with Toeplitz covariance matrix $R_H(l) = (r_H(|i-j|))_{0 \le i,j \le l-1}$. One can embed $R_H(l)$ in a circulant matrix of size $2l$ given by $S_H(l) = \text{circ}(s_H(l))$ with $s_H(l) = (r_H(0), \ldots r_H(l-1) r_H(l-2), \ldots r_H(1))$. The main interesting property of circulant matrices is that they are diagonalized in the discrete Fourier basis, with their eigenvalues given by the Discrete Fourier Transform of their first row. In particular one has

$$S_H(l) = \frac{1}{2l} F_{2l}^* \text{diag}(F_{2l} s_H(l)) F_{2l}, \quad \text{where} \quad F_{2l} = (e^{\frac{i\pi jk}{l}})_{0 \le i,j \le 2l-1}.$$

The main results of [35] is that for all $H \in (0,1)$ and $l \geq 1$, $F_{2l}s_H(l)$ always has positive entries, so that $S_H(l)$ is a covariance matrix. Moreover, if $\varepsilon_{2l}^{(1)}$ and $\varepsilon_{2l}^{(2)}$ are independent vectors of law $\mathcal{N}(0, I_{2p})$ the vectors $Z^{(1)} = \frac{1}{\sqrt{2l}}\Re\left(F_{2l}^* \mathrm{diag}(F_{2l}s_H(l))^{1/2}(\varepsilon_{2l}^{(1)} + i\varepsilon_{2l}^{(1)})\right)$ and $Z^{(2)} = \frac{1}{\sqrt{2l}}\Im\left(F_{2l}^* \mathrm{diag}(F_{2l}s_H(l))^{1/2}(\varepsilon_{2l}^{(1)} + i\varepsilon_{2l}^{(2)})\right)$ are independent with common law $\mathcal{N}(0, S_H(l))$. In particular, one has $(Z_H(0), \ldots, Z_H(l-1)) \stackrel{d}{=} (Z_0^{(i)}, \ldots, Z_{l-1}^{(i)})$ for $i = 1, 2$ and using stationarity of the increments of B_H and the fact that $B_H(0) = 0$ a.s., one has, for all $m \leq l$,

$$(B_H(k))_{-m \leq k \leq l-m} = \left(\sum_{j<k+m} Z_H(j) - \sum_{j<m} Z_H(j)\right)_{-m \leq k \leq l-m},$$

with the convention that $\sum_{j<0} = 0$. Let us emphasize that this procedure is very fast since, choosing l as a power of 2, the cost is reduced to $O(l\log(l))$ using the Fast Fourier Transform algorithm.

3.2. **Choice of bands.** We consider the exact simulation of $X_{\Theta,\Lambda}$ on the discrete grid $r^{-1}\mathbb{Z}^2 \cap [0,1]^2$ for some $r \geq 1$. Then for any i with $1 \leq i \leq n$ we have to simulate on each band of direction $u(\theta_i)$

$$\left\{Y_i(x \cdot u(\theta_i)); x \in r^{-1}\mathbb{Z}^2 \cap [0,1]^2\right\} = \left\{Y_i\left(\frac{k_1}{r}\cos(\theta_i) + \frac{k_2}{r}\sin(\theta_i)\right); 0 \leq k_1, k_2 \leq r\right\}.$$

Note that when $\theta_i = \pi/2$ we can simply use the fact that $\left\{Y_i\left(\frac{k_2}{r}\right); 0 \leq k_2 \leq r\right\} \stackrel{d}{=} r^{-h(\theta_i)}\left\{Y_i(k_2); 0 \leq k_2 \leq r\right\}$, by self-similarity. When $\cos(\theta_i) \neq 0$ we may choose θ_i such that $\tan\theta_i = \frac{p_i}{q_i}$, with $p_i \in \mathbb{Z}$ and $q_i \in \mathbb{N}$ and use that fact that

$$\left\{Y_i\left(\frac{k_1}{r}\cos(\theta_i) + \frac{k_2}{r}\sin(\theta_i)\right); 0 \leq k_1, k_2 \leq r\right\}$$

$$\stackrel{d}{=} \left(\frac{\cos(\theta_i)}{rq_i}\right)^{h(\theta_i)}\left\{Y_i(k_1q_i + k_2p_i); 0 \leq k_1, k_2 \leq r\right\}.$$

Thus, the band with direction $u(\theta_i)$ involves the simulation of a 1D fractionnal Brownian motion on a discrete interval of length $r(|p_i| + q_i)$. The computational cost of this simulation is $O(C(|p_i| + q_i))$, where $O(C(l))$ is the computational cost of the Fourier Transform

used in the procedure described in Section 3.1 to simulate a 1D fractional Brownian motion on the discrete interval $\{0, \dots, rl\}$. If the Fast Fourier Transform with powers of two is used, then one has $C(l) = 2^{\lceil \log_2(rl) \rceil} \lceil \log_2(rl) \rceil$, where $\lceil x \rceil$ denotes the upper integer part of x. Finally, the overall simulation process has to find a trade-off between the computational cost

$$\mathcal{C}(\Theta) = \sum_i C(|p_i| + q_i)$$

and the precision of the simulation, which is controlled by $\mathcal{E}(\Theta) = \varepsilon_\Theta^{\min(2H,1)}$. The optimal choice of Θ is discussed in the following section.

3.3. **Band selection by Dynamic Programming.** As we just saw in the previous section, we need to restrain our choice of band orientations to angles θ that correspond to vectors (q, p) with integer coordinates, that is, such that $\tan \theta = \frac{p}{q}$. Moreover, in order to control the total computational cost, we would like to favor small factors (small values of $|p| + q$) while controlling the repartition of bands in order to keep ε_Θ small. A simple (but non-optimal) solution to select the set of angles $\Theta = (\theta_i)_i$ consists in using a uniform discretization $\tilde{\theta}_i = \alpha_1 + \frac{i}{n}(\alpha_2 - \alpha_1)$, then choosing for each i a rational approximation $\frac{p_i}{q_i}$ of $\tan \tilde{\theta}_i$ (this can be done very efficiently using the appropriate convergent of the continued fraction associated to $\tan \tilde{\theta}_i$). However, as we shall see now, one can find a simple algorithm, based on Dynamic Programming [4], that is able to select a set of angles Θ that minimizes the computational cost $\mathcal{C}(\Theta)$ under the error control constraint $\varepsilon_\Theta \leq \varepsilon$. In practice, we restrain our choice to angles that can be written under the form $\theta = \angle(q, p)$, where (p, q) belongs to

$$\mathcal{V}_N = \{(p, q); \ -N \leq p \leq N, 1 \leq q \leq N, \gcd(p, q) = 1, \alpha_1 < \angle(q, p) < \alpha_2\}$$

and $\angle(q, p)$ is the measure in $[-\frac{\pi}{2}, \frac{\pi}{2}]$ of the angle of the vector (q, p), obtained by $\angle(q, p) = \arctan \frac{p}{q}$. The integer N should be chosen large enough to ensure that the optimal solution only involves vectors from $\mathcal{V}_N$. It seems that choosing $N = 1 + \left\lceil \frac{1}{\tan \varepsilon} \right\rceil$ (so that $\angle(N, 1) < \varepsilon$) is enough, though we do not have a proof of this (even if this were

not true, the algorithm we present here would yield slightly sub-optimal sets of bands, with little practical consequences).

Now assume that the set $\mathcal{V}_N$ has been sorted into a sequence $(p_k, q_k)_{1 \leq k \leq n}$ such that the associated angular sequence $\theta_k = \angle(q_k, p_k)$ is increasing. Writing $e_k = C(r(|p_k| + q_k))$ the elementary cost associated to a band with orientation θ_k, we can rewrite the total computational cost of a set of angles $\Theta = (\theta_{i_k})_{1 \leq k \leq s}$ as

$$C(\Theta) = \sum_{k=1}^{s} e_{i_k}.$$

We add the convention that $\theta_{n+1} = \alpha_2$ and $\theta_0 = \alpha_1$ (with the associated elementary cost $e_0 = 0$). Now, for $0 \leq i \leq n+1$, let us call c_i the minimal cost that can be realized with a sequence $i_1 = i, i_2, \ldots i_s = n+1$ for some integer s. Then, c_0 is the optimal cost we look for, and for all $0 \leq i \leq n$ we have

(22)
$$c_i = e_i + \min_{j;\, j>i,\, \theta_j \leq \theta_i + \varepsilon} c_j.$$

This induction formula (called Bellman Equation in the framework of Dynamic Programming) permits us to compute the optimal costs $c_n, c_{n-1}, \ldots c_0$ recursively (the initialization being made with $c_{n+1} = 0$). Moreover, each time the minimum in (22) is computed, we consider one optimal index

$$k_i \in \arg \min_{j;\, j>i,\, \theta_j \leq \theta_i + \varepsilon} c_j,$$

then an optimal sequence $i_1, i_2, \ldots i_s$ can be computed by tracking back indexes that achieve the optimal cost c_0. This sequence is given by

$$i_1 = k_0, i_2 = k_{i_1}, \ldots i_s = k_{i_{s-1}},$$

where the value of s is obtained using the fact that $i_{s+1} = n + 1$. In the end, the desired sequence of integer vectors is simply $(\bar{p}_k, \bar{q}_k)_{1 \leq k \leq s}$, where $(\bar{p}_k, \bar{q}_k) = (p_{i_k}, q_{i_k})$ for all $1 \leq k \leq s$. The whole procedure we just described is given in pseudo-code in Algorithm 1 of Appendix C.
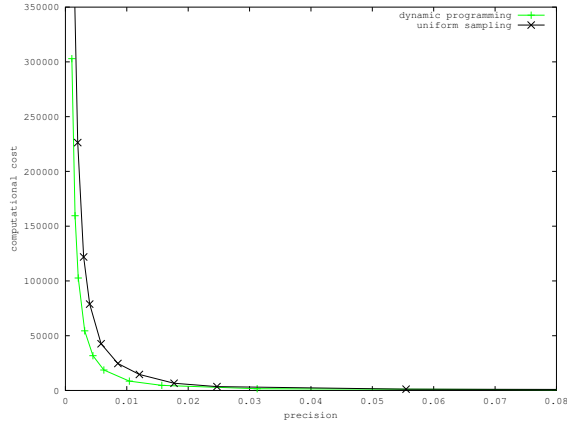
FIGURE 1. Comparison of an approximate uniform sampling of turning bands and their selection by dynamic programming.

4. NUMERICAL STUDY

This section is devoted to the numerical evaluation of anisotropic fractional Brownian field (AFBF) simulations obtained by turning bands.

Let us recall some notations. The field X is the theoretical field to be simulated (AFBF). Its variogram v_X is of the form (1) with a spectral density defined by (2). The field $X_{\Theta,\Lambda}$ is the turning-band simulation field defined by Equation (11) for some sets Θ and Λ giving band orientations and weights, respectively. The variogram $v_{\Theta,\Lambda}$ of $X_{\Theta,\Lambda}$ is defined by Equation (14).

In all experiments, the set Θ of band orientations was computed automatically using the Dynamic Programming algorithm described in Section C with a constraint on field precision. The precision parameter ε_Θ associated to the set Θ is defined as in Equation (12). Weights λ_i of Λ are defined to fullfil the condition (16) of Proposition 2.4.
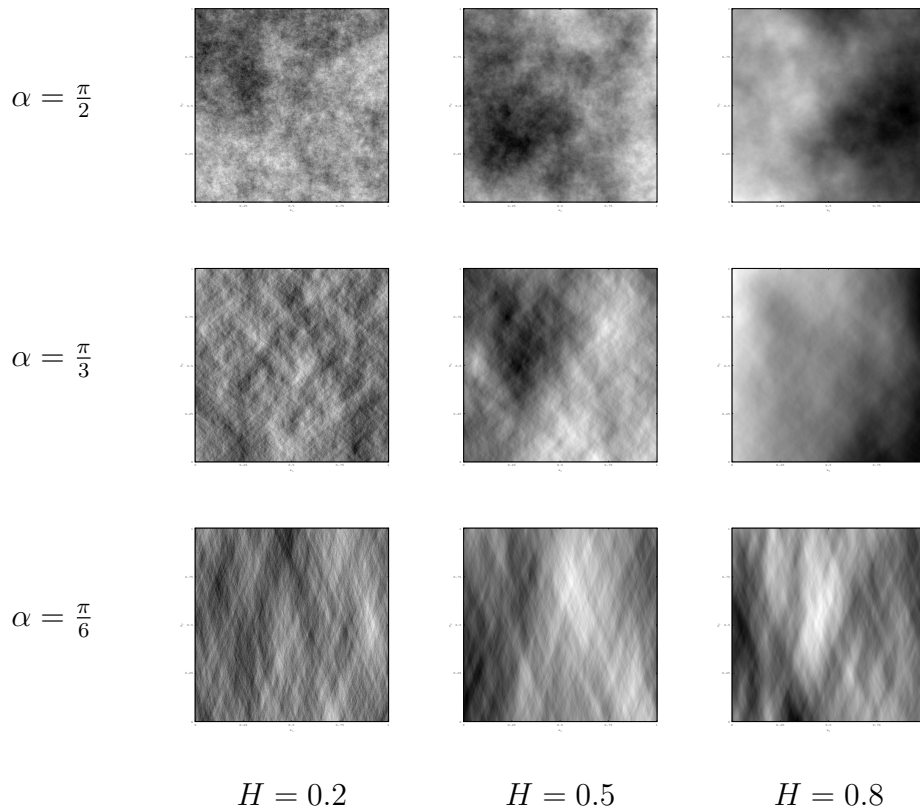
FIGURE 2. Realizations on $[0,1]^2$ of elementary fields obtained for different values of H and α using the TBM with 5900 bands.

4.1. **The use of elementary fields.** Our evaluation was focused on elementary fields whose spectral density is given by Equation (2) taking $h \equiv H$ for some $H \in (0,1)$ and $c = \mathbf{1}_{[-\alpha,\alpha]}$ for some $0 < \alpha \leq \pi/2$.

Elementary fields are specified by only two parameters, H and α, which can be interpreted as regularity and anisotropy parameters, respectively. The Hölder regularity of these fields being equal to H (see [9] for instance), it increases as H tends to 1. When $\alpha = \pi/2$, elementary fields correspond to usual isotropic fractional Brownian fields of Hurst index H. When $0 < \alpha < \pi/2$, these fields are no longer isotropic. In this case, they are some kind of fractional Brownian fields whose non-null frequency components are restricted between frequency directions $-\alpha$ and α. As α decreases to 0, non-null field frequency components become more and more focused around the horizontal direction.

On Figure 2, some elementary field realizations are shown for illustrating both the effect of increasing H on the field regularity and the effect of decreasing α on its anisotropy. For the evaluation, we considered elementary fields of varying degrees of regularity and anisotropy, taking all parameter pairs (H, α) for H in $\{0.2, 0.5, 0.8\}$ and α in $\{\pi/6, \pi/3, \pi/2\}$.

Let us further mention that variograms of elementary fields can be computed using the closed form given in Equation (9). As it will appear next, this is of particular interest for the computation of evaluation criteria. On Figure 3, some of these variograms are presented for different degrees of regularity and anisotropy.
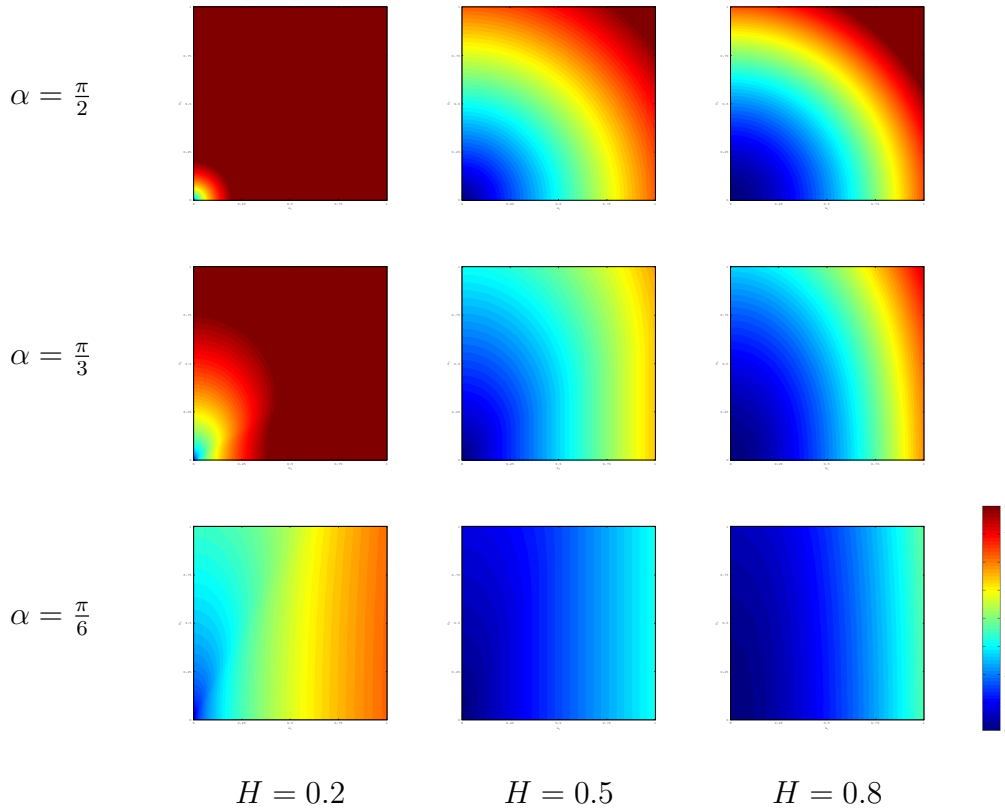

FIGURE 3. Variograms on $[0, 1]^2$ of elementary fields for different values of H and α.

Finally, let us notice that any anisotropic fractional Brownian field whose spectral density is defined with piecewise constant functions h and c can be decomposed as a

sum of independent elementary fields. Hence, although achieved on elementary fields, our evaluation accounts for more general anisotropic fractional Brownian fields.

4.2. **Approximation error.** As mentionned in Section 2.3, simulation errors result from the distance separating simulation and theoretical fields. This distance can be defined as the Kolmogorov distance between distributions of theoretical and simulation fields at each position x. As stated in Theorem 2.3 (Equation (15)), the Kolmogorov distance is further bounded by $d_{\Theta,\Lambda}(x) = \frac{|v_X(x) - v_{\Theta,\Lambda}(x)|}{v_X(x)}$, which is proportional to the error made when approximating the variogram of X by the one of $X_{\Theta,\Lambda}$. Moreover, when X is an elementary field, it is possible to compute the bound $d_{\Theta,\Lambda}(x)$ using closed forms of $v_{\Theta,\Lambda}(x)$ and $v_X(x)$ given by Equations (14) and (9), respectively. Hence, using elementary fields, we could numerically evaluate a simulation error by averaging values of $d_{\Theta,\Lambda}(x)$ over points x of a uniform subgrid of $[0,1]^2$:

$$(23) \qquad d_{\Theta,\Lambda} = \sum_{k,l=1}^{p} d_{\Theta,\Lambda}\left(\frac{k}{p}, \frac{l}{p}\right) = \sum_{k,l=1}^{p} \frac{|v_X(\frac{k}{p}, \frac{l}{p}) - v_{\Theta,\Lambda}(\frac{k}{p}, \frac{l}{p})|}{v_X(\frac{k}{p}, \frac{l}{p})}, \text{ with } p = 64.$$

As this is evidenced by Equation (17) of Proposition 2.4, the measured error $d_{\Theta,\Lambda}$ depends on the precision parameter ε_Θ of the simulation field. Figure 4 illustrates the effect of increasing ε_Θ (*i.e* reducing the simulation precision) on simulations of a fractional Brownian field of Hurst index $H = 0.2$. When the precision becomes too low ($\varepsilon_\Theta \geq 0.25$), field realizations have some stripes in different directions, and simulation field variograms present some singularities on lines radiating from the origin. This well-known effect, often called artifact banding in the literature [24, 31, 21, 20], is due to the fact that the contribution of a band process Y_i to the sum defining the simulation field (see Equation (11)) is null for points on the line orthogonal to the band direction θ_i and passing through origin.

On Figure 5, we plotted values of error bounds $d_{\Theta,\Lambda}$ obtained for different elementary fields as a function of the precision parameter ε_Θ. Whatever the field parameters, error bounds varied almost linearly with respect to ε_Θ. They did not seem to depend on the regularity parameter H. However, they were slightly dependent on the anisotropy
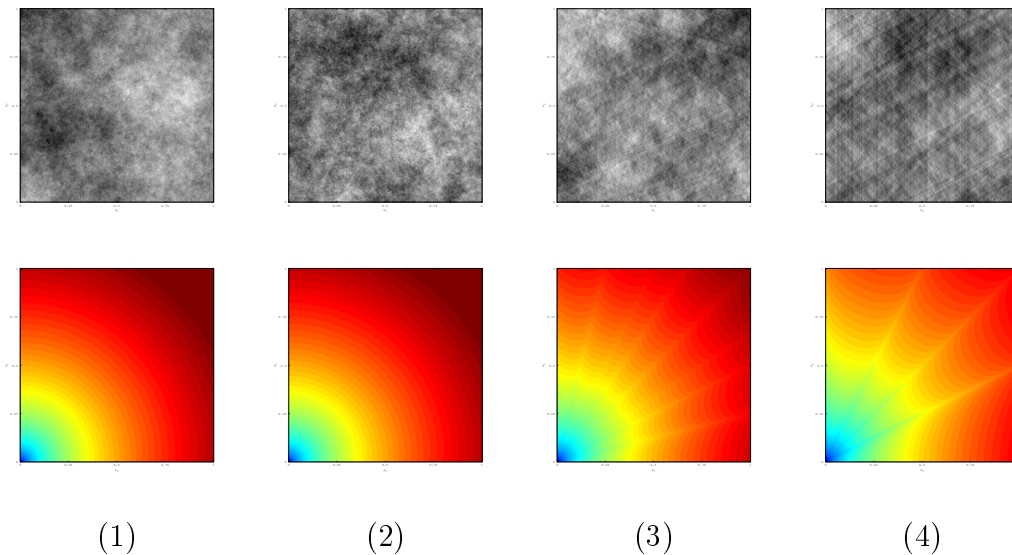
FIGURE 4. Effect of reducing the field precision on simulations of a fractional Brownian field of Hurst index $H = 0.2$. On the first row, realizations of simulation fields $X_{\Theta,\Lambda}$ of decreasing precision and, on the second row, corresponding variograms: (1) $\varepsilon_\Theta = 0.04$ ($n = 103$), (2) $\varepsilon_\Theta = 0.077$ ($n = 51$), (3) $\varepsilon_\Theta = 0.25$ ($n = 15$) and (4) $\varepsilon_\Theta = 0.464$ ($n = 7$).

parameter α, especially at low precision ($\varepsilon_\Theta > 0.03$). Error bounds of all fields fell below 1% when $\varepsilon_\Theta < 0.02$, such a precision being reached with around 150 simulation bands.

4.3. **Estimation error.** We also conducted numerical experiments to evaluate errors which arise when estimating field features (*e.g.* parameters, variograms) from field simulations.

Applying the TBM (with 1321 bands on a 64×64 grid of $[0,1]^2$), we simulated 2000 independent realizations $\{y^{(k)}, k = 1, \cdots, 2000\}$ of a given elementary field X of variogram v_X. Given $k \in \{1, \cdots, 2000\}$, we then computed the empirical variogram $v^{(K)}(x)$ at position x using the K first samples:
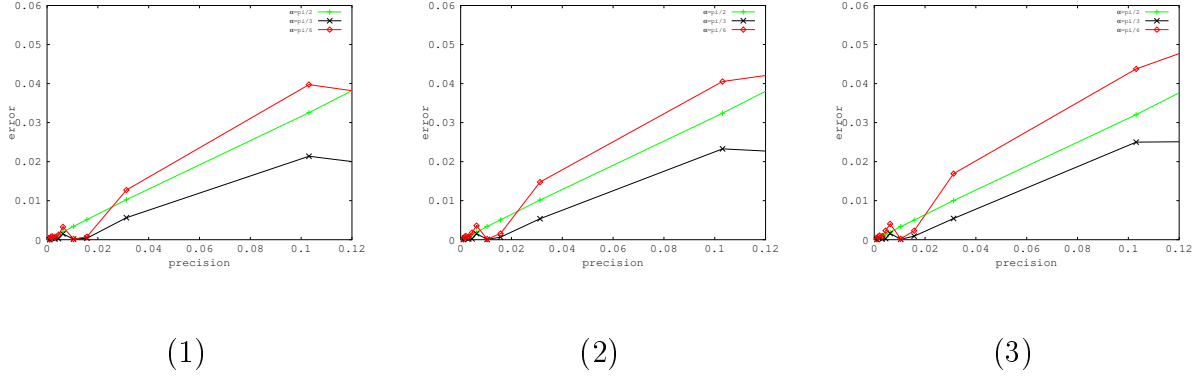
$$v^{(K)}(x) = \frac{1}{2K} \sum_{k=1}^{K} (y^{(k)}(x))^2.$$

| (1) | (2) | (3) |

FIGURE 5. Variations of the error bound $d_{\Theta,\Lambda}$ relative to the precision parameter ε_Θ for elementary fields with different values of H and α: (1) $H = 0.2$, (2) $H = 0.5$, (3) $H = 0.8$.

Finally, we computed an estimation error $d^{(K)}(x) = \frac{|v_X(x) - v^{(K)}|}{v_X(x)}$ at point x, and its average over points x of the grid

$$(24) \qquad d^{(K)} = \sum_{k,l=1}^{p} d^{(K)}\left(\frac{k}{p}, \frac{l}{p}\right) = \sum_{k,l=1}^{p} \frac{|v_X(\frac{k}{p}, \frac{l}{p}) - v^{(K)}(\frac{k}{p}, \frac{l}{p})|}{v_X(\frac{k}{p}, \frac{l}{p})}, \text{ with } p = 64.$$

On Figure 6, some empirical variograms $v^{(K)}$ estimated from simulations of a fractional Brownian field of Hurst index $H = 0.2$ are compared to the theoretical variogram v_X of X. This illustrates both the convergence of empirical variograms to the theoretical one as K tends to $+\infty$, and estimation errors due to the lack of samples.

On Figure 7, we plotted the estimation error $d^{(K)}$ as a function of the sample number K for different elementary fields. For a same value of the regularity parameter H, the convergence of the error to zero is about the same for all values of the anisotropy parameter α. However, the convergence gets slower and slower as H increases. In all cases, around 1000 samples are required for the error to get below 5%.

Besides, we built a statistical test to check the adequacy of simulations to the model. For any position x, let $Y^{(1)}(x), \cdots, Y^{(K)}(x)$ be independent and identically distributed
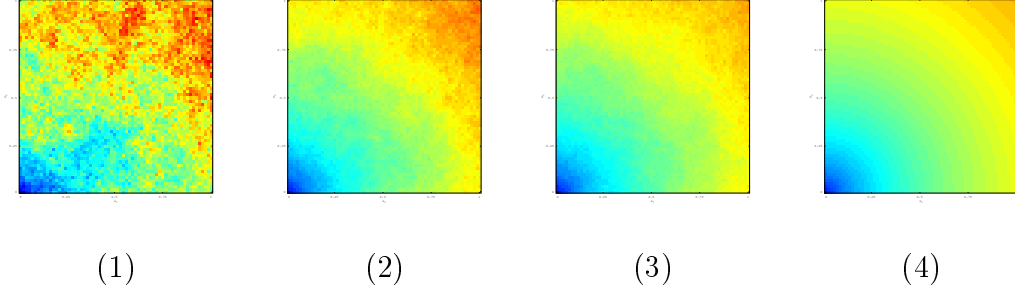
(1) (2) (3) (4)

FIGURE 6. Effect of increasing the number of samples on simulations of a fractional Brownian field of Hurst index $H = 0.2$ (simulations were done with 1321 bands on a 64×64 grid of $[0,1]^2$): Empirical variograms $v^{(K)}$ computed with (1) $K = 60$, (2) $K = 1000$, (3) $K = 2000$ samples, and (4) theoretical variogram.
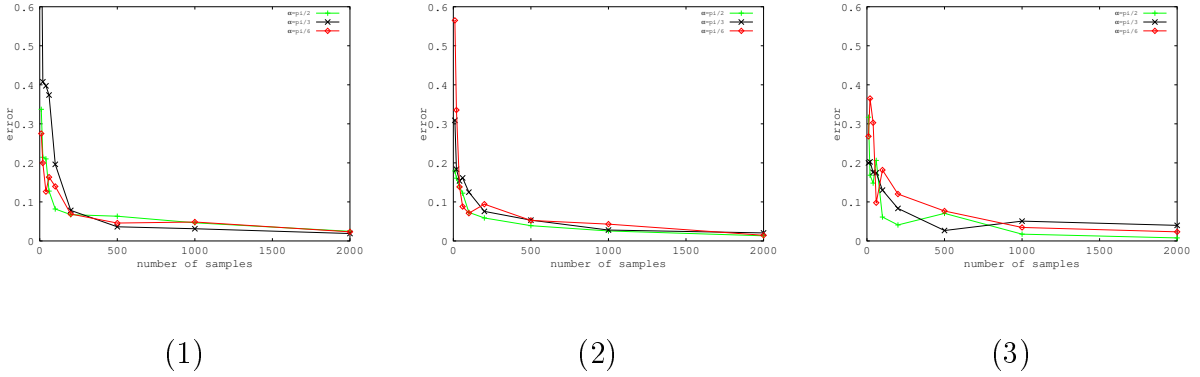

(1) (2) (3)

FIGURE 7. Variations of the estimation error relative to the number K of samples for elementary fields with different values of H and α: (1) $H = 0.2$, (2) $H = 0.5$, (3) $H = 0.8$.

random variables, and $\mathcal{H}_0^x$ be the hypothesis that their distribution is the same as the one of $X(x)$, *i.e.* a centered gaussian distribution with variance $2v_X(x)$. For testing $\mathcal{H}_0^x$, we define the rejection interval $\{D^{(K)}(x) > c\}$, where the statistic $D^{(K)}(x) = \frac{|V^{(K)}(x) - v_X(x)|}{v_X(x)}$ with $V^{(K)}(x) = \frac{1}{2K} \sum_{k=1}^{K} (Y^{(k)}(x))^2$. Under assumption $\mathcal{H}_0^x$, $K \frac{V^{(K)}(x)}{v_X(x)}$ has a χ^2 distribution

of degree K. Hence, under $\mathcal{H}_0^x$, the probability of the rejection interval can be computed, and the rejection bound c can be set according to a level of test. Given a realization $d^{(k)}(x)$ of $D^{(K)}(x)$, it also possible to evaluate the p-value $p^{(K)}(x)$ of the test (*i.e* the minimal risk of rejecting $\mathcal{H}_0^x$) as

$$p^{(K)}(x) = 1 - P(Z^{(K)} < K(d^{(k)}(x) + 1)) + P(Z^{(K)} < K(-d^{(k)}(x) + 1)),$$

where $Z^{(K)}$ is a χ_K^2 random variable.

To evaluate the simulation-to-model adequacy, we computed for different K the average $p^{(K)}$ of p-values $p^{(K)}(x)$ at positions x of the 64×64 grid of $[0,1]^2$. On Figure 8, the mean p-values are plotted as a function of the sample number K. Whatever the value of parameters H and α, mean p-values are all above 0.3, indicating that hypotheses $\mathcal{H}_0^x$ of adequacy are not rejected at low risks. Besides, the mean p-values seems to reach an upper bound which is below 1 (around 0.5). This is probably due to both the approximation error and estimator inacurracy.
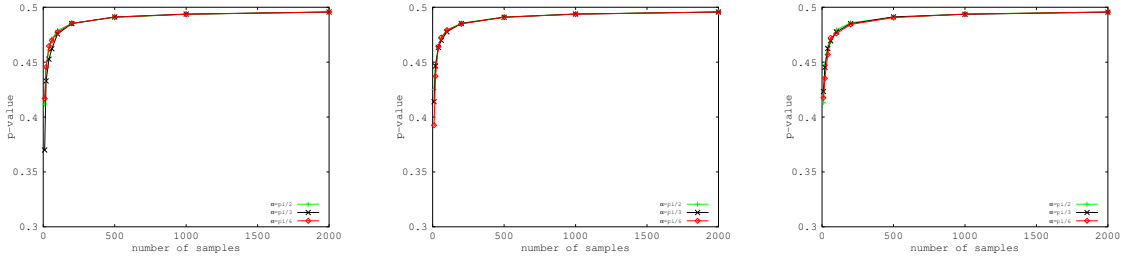
(1)   (2)   (3)

FIGURE 8. Mean p-values $p^{(K)}$ of adequacy tests relative to the number K of samples for elementary fields with different values of H and α: (1) $H = 0.2$, (2) $H = 0.5$, (3) $H = 0.8$.

5. DISCUSSION

We have constructed turning-band fields suited to the simulation of AFBF. This construction is based on the resolution of an integral equation specific to the non-stationary anisotropic context of AFBF. This ensures the convergence of simulation fields to target fields as the precision increases. Moreover, the band processes involved in the definition of simulation fields are simulated exactly using a circulant embedding method. Hence, errors produced by the simulation method are exclusively due to the approximation of the target field by the simulation field. This approximation error was evaluated theoretically and numerically. From a numerical point of view, we observed that it does not depend significantly on the regularity of target fields, nor on their degree of anisotropy. Experiments have also suggested that simulations preserve the statistical properties of the target field. Besides, we obtained good simulation results with few bands (around 150) at a low computational cost.

The evaluation was achieved on some elementary fields. However, simulation possibilities offered by the TBM go far beyond those fields, as there is a large choice of parameter definitions and tunings. Using the TBM, it chiefly becomes possible to visualize truthfully realizations of different anisotropic field models studied in the literature [9, 6, 16, 36]. In the generic model defined by Equation (2), we recall that the field anisotropy is introduced through two direction-dependent and π-periodic functions: the Hurst index function h and the topothesy function c. So as to illustrate the effect of varying these parameter functions, we considered three functions of increasing regularity:

- a discontinuous function g_1: for $\mu_1, \mu_2 \in (0,1)$, $g_1(\omega) = \mu_1$ if $\omega \in (-\frac{\pi}{4}, \frac{\pi}{4})$ and $g_1(\omega) = \mu_2$ if $\omega \in (-\pi, \pi) \backslash (-\frac{\pi}{4}, \frac{\pi}{4})$,
- a continuous but not differentiable function g_2: for $\mu_1, \mu_2 \in (0,1)$, $g_2(0) = \mu_1$, $g_2(-\pi/2) = g(\pi/2) = \mu_2$, and g_2 is piecewise linear on $(-\pi/2, 0)$ and $(0, \pi/2)$.
- an infinitely differentiable function g_3: $g_3(\omega) = \mu_1 r(\omega) + \mu_2 (1 - r(\omega))$ with $r(\omega) = (1 + \sin(2\omega + \pi/2))/2$ for $\omega \in [0, \pi/2]$, and $g_3(\omega) = g_3(-\omega)$ for $\omega \in [-\pi/2, 0]$.

Fixing the topothesy function to a constant ($c \equiv 1$), we first simulated field realizations with Hurst index functions $h = g_i$ for $i = 1, 2, 3$ and different pairs of parameter values (μ_1, μ_2); results are shown on Figure 9. In these realizations, the degree of anisotropy can be measured as the difference $\mu_2 - \mu_1$ between maximal and minimal Hurst indices. It is the same for realizations of the first and second columns ($\mu_2 - \mu_1 = 0.3$), and higher for those of the third column ($\mu_2 - \mu_1 = 0.5$). Moreover, the Hölder regularity of those realizations is equal to μ_1. It is the same for realizations of the first and third columns ($\mu = 0.2$) and higher for those of the second column ($\mu = 0.5$). Comparing realizations on a same row, we clearly see the effect of anisotropy and regularity variations on field textures: as the field regularity decreases, the texture gets rougher, and, as the field anisotropy increases, texture patterns get more obviously oriented. Besides, comparing realizations on a same column, we can observe texture differences induced by changing the regularity of the Hurst index function h in the model. In particular, realizations obtained with a discontinous function h (on the first row) have some linear patterns which are not present on those obtained with a more regular function h (on the second and third rows).

Fixing the Hurst index function to a constant ($h \equiv 0.5$), we also simulated field realizations with topothesy functions $c = g_i$ for $i = 1, 2, 3$ and different pairs of parameter values (μ_1, μ_2); results are shown on Figure 10. In these realizations, the degree of anisotropy can be defined as the difference $\mu_2 - \mu_1$ between maximal and minimal topothesy values. From a column to the next one, it is increased, while the field regularity remains the same for all realizations ($H = 0.2$). As it can be observed by comparing realizations on a same row, variations of the anisotropy degree cannot be visually detected on textures. However, comparing realizations on a same column, we can notice that the regularity of the topothesy function has an effect on the field texture. As previously, some line patterns are present on textures when the topothesy function is discontinous.

In the simulations we presented, field realizations were generated on a regular subgrid of $[0, 1]^2$. Using our TBM approach, it is however possible to simulate fields on other sets of non-uniformly spaced positions. To do so, the only condition is that position coordinates
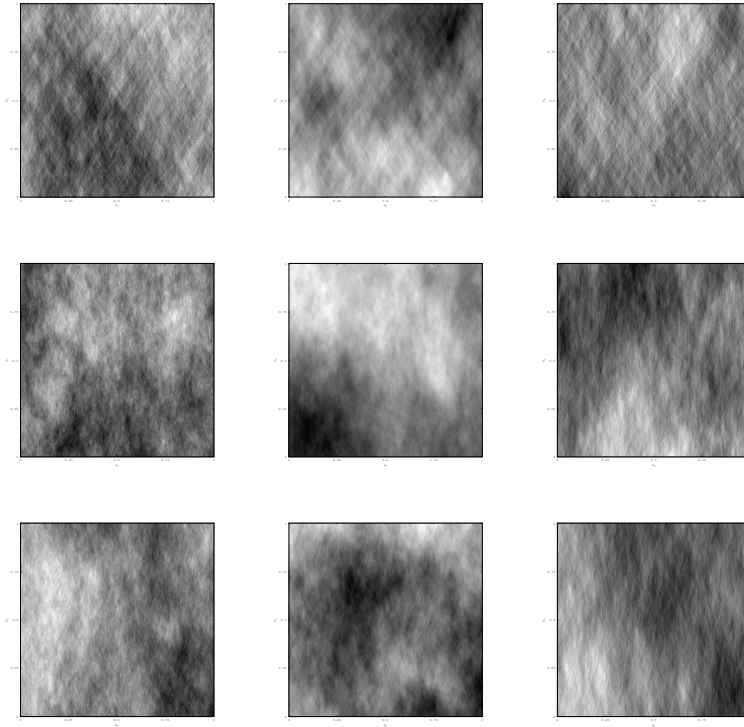
FIGURE 9. Field realizations obtained with different Hurst index functions h. For all realizations, the topothesy function $c \equiv 1$. On the first, second and third rows, Hurst index functions are $h = g_1$ (discontinuous), $h = g_2$ (continuous but not differentiable), and $h = g_3$ (infinitely differentiable), respectively. On the first, second and third columns, Hurst index functions are specified by parameter pair values $(\mu_1, \mu_2) = (0.2, 0.5)$, $(\mu_1, \mu_2) = (0.5, 0.8)$, and $(\mu_1, \mu_2) = (0.2, 0.8)$, respectively.

are all rational; this is required for the exact simulation of fractional Brownian motions on turning bands (refer to Section 3.1). The pseudo-polar grid is an example of a set of points satisfying this simulation condition [1]. Such a grid is of particular interest for computing discrete Radon transforms [2], as its points are uniformly spread on different lines radiating from the origin. But Radon transforms are one of the key features for the construction of parameter estimators for AFBF [7, 36]. Hence, those estimators could be better discretized and evaluated using simulations on a pseudo-polar grid.
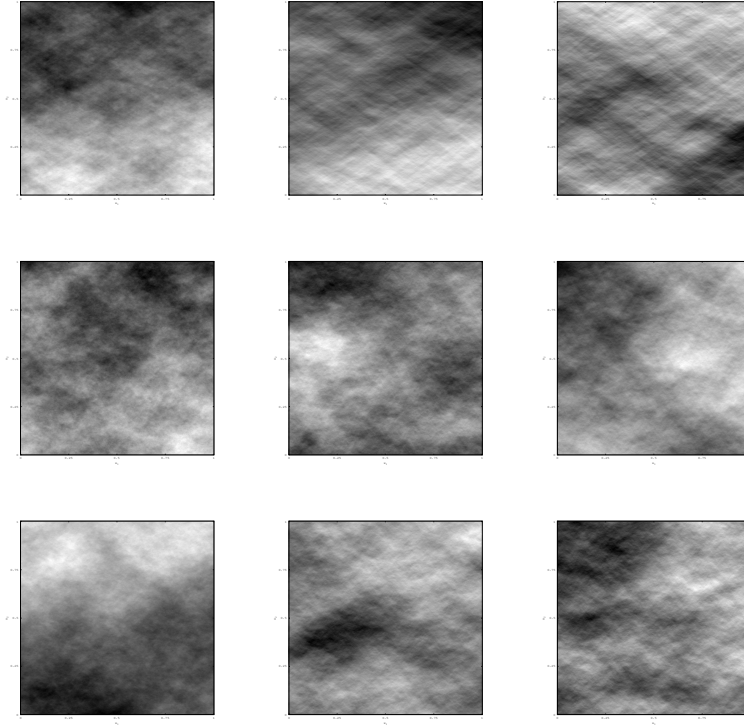
FIGURE 10. Field realizations obtained with different topothesy functions. For all realizations, the Hurst index function $h \equiv 0.2$. On the first, second and third rows, topothesy functions are $c = g_1$ (discontinuous), $c = g_2$ (continuous but not differentiable), and $c = g_3$ (infinitely differentiable), respectively. On the first, second and third columns, topothesy functions are specified by parameter pair values $(\mu_1, \mu_2) = (1, 5)$, $(\mu_1, \mu_2) = (1, 100)$, and $(\mu_1, \mu_2) = (1, 1000)$, respectively.

Due to the ability of the TBM to simulate fields on quasi-arbitrary points, it also becomes possible to simulate field deformations. For instance, let A be the 2×2-matrix of an affine transform (with rational components) and $\tilde{X} = X \circ A$ the deformation of the random field X by the affine transform A. Realization of $\tilde{X}$ on a uniform grid G of $[0, 1]^2$ can be obtained by applying the TBM to the simulation of X on $\{Ax, x \in G\}$. Figure 11 presents an illustration corresponding to the deformation of a fractional Brownian field of

Hurst index $H = 0.5$ by a shear in the horizontal direction, that is, $A = \begin{pmatrix} 1 & 2 \\ 0 & 1 \end{pmatrix}$. This example also shows that deformating isotropic fields is a means to construct anisotropic fields.
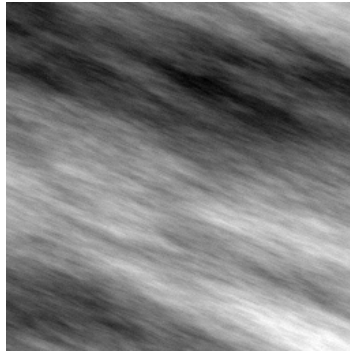

FIGURE 11. Shear of a fractional Brownian field of Hurst index 0.5.

Simulation is a central issue concerning the investigation of anisotropic fields. As shown previously, a simulation technique such as the TBM can serve as a tool for visualizing mathematical properties of anisotropic models under study. From an application viewpoint, it can also help assessing the similarity between model realizations and real-world images. Besides, having reliable simulations is critical for the evaluation of model parameter estimators. In future works, we plan to use TBM simulations of AFBF to evaluate the estimators we constructed using quadratic variations [7, 36]. We also intend to use those simulations to refine the adequacy between models and radiographic images we analyze for the characterization of osteoporosis and breast cancer [5, 8, 36].

APPENDIX A. PROOF OF PROPOSITION 2.1

Proof. According to Proposition 2.2, for all $x \in \mathbb{R}^2$,

$$
\begin{aligned}
v_{H,\alpha_1,\alpha_2}(x) &= \frac{1}{2} \int_{-\pi/2}^{\pi/2} \gamma(h(\theta)) c(\theta) |x \cdot u(\theta)|^{2h(\theta)} d\theta \\
&= \frac{1}{2} \gamma(H) \|x\|^{2H} \int_{\alpha_1}^{\alpha_2} |\cos(\theta - arg(x))|^{2H} d\theta.
\end{aligned}
$$

We will use the following lemma.

Lemma A.1. *Let $a, b \in \mathbb{R}$ with $-\pi/2 \le a < b \le \pi/2$, then*

$$
\int_a^b |\cos(\theta)|^{2H} d\theta = 2^{2H} \left(\beta_H \left(\frac{1 + \sin(b)}{2} \right) - \beta_H \left(\frac{1 + \sin(a)}{2} \right) \right).
$$

Proof. Since we assume that $-\pi/2 \le a < b \le \pi/2$,

$$
\begin{aligned}
\int_a^b |\cos(\theta)|^{2H} d\theta &= \int_a^b \left(1 - \sin(\theta)^2 \right)^{H-1/2} \cos(\theta) d\theta \\
&= \int_{\sin(a)}^{\sin(b)} (1 - u^2)^{H-1/2} du,
\end{aligned}
$$

by the change of variables $u = \sin(\theta)$. Then, by the change of variables $v = \frac{1+u}{2}$, we obtain

$$
\int_a^b |\cos(\theta)|^{2H} d\theta = 2^{2H} \int_{\frac{1+\sin(a)}{2}}^{\frac{1+\sin(b)}{2}} (1-v)^{H-1/2} v^{H-1/2} dv,
$$

which gives the result. $\qquad \square$

This allows us to get the next result, which concludes the proof.

Corollary A.2. *Let $a, b \in \mathbb{R}$ with $0 \le b - a \le \pi$, then*

$$
\int_a^b |\cos(\theta)|^{2H} d\theta = 2^{2H}
\begin{cases}
\left| \beta_H \left(\frac{1+\sin(b)}{2} \right) - \beta_H \left(\frac{1+\sin(a)}{2} \right) \right| & if \quad (a,b) \cap \frac{\pi}{2} + \mathbb{Z}\pi = \emptyset \\
\beta_H \left(\frac{1+\sin(b)}{2} \right) + \beta_H \left(\frac{1+\sin(a)}{2} \right) & if \quad (a,b) \cap -\frac{\pi}{2} + 2\mathbb{Z}\pi \ne \emptyset \\
\beta_H \left(\frac{1-\sin(b)}{2} \right) + \beta_H \left(\frac{1-\sin(a)}{2} \right) & if \quad (a,b) \cap \frac{\pi}{2} + 2\mathbb{Z}\pi \ne \emptyset
\end{cases}
$$

Proof. We first assume that $(a, b) \cap \frac{\pi}{2} + \mathbb{Z}\pi = \emptyset$. Since $0 \le b - a \le \pi$, one can find $k \in \mathbb{Z}$ such that $-\pi/2 \le a + k\pi < b + k\pi \le \pi/2$. The result follows from Lemma A.1 when k is even. When k is odd,

$$\int_a^b |\cos(\theta)|^{2H} d\theta = \int_{a+k\pi}^{b+k\pi} |\cos(\theta)|^{2H} d\theta = 2^{2H} \left(\beta_H \left(\frac{1 - \sin(b)}{2} \right) - \beta_H \left(\frac{1 - \sin(a)}{2} \right) \right),$$

according to Lemma A.1. Note that by a change of variables, for all $\theta \in \mathbb{R}$

$$(25) \qquad \beta_H \left(\frac{1 - \sin(\theta)}{2} \right) = \beta_H(1) - \beta_H \left(\frac{1 + \sin(\theta)}{2} \right)$$

and the result follows.

Let assume that $-\frac{\pi}{2} + 2\mathbb{Z}\pi \ne \emptyset$. Then, one can find $k \in \mathbb{Z}$ such that $a + 2k\pi < -\pi/2 < b + 2k\pi$, and according to Lemma A.1,

$$\begin{aligned}
\int_a^b |\cos(\theta)|^{2H} d\theta &= \int_{a+2k\pi}^{b+2k\pi} |\cos(\theta)|^{2H} d\theta \\
&= \int_{a+2k\pi}^{-\pi/2} |\cos(\theta)|^{2H} d\theta + \int_{\pi/2}^{b+2k\pi} |\cos(\theta)|^{2H} d\theta \\
&= \int_{a+\pi+2k\pi}^{\pi/2} |\cos(\theta)|^{2H} d\theta + 2^{2H} \beta_H \left(\frac{1 + \sin(b)}{2} \right) \\
&= 2^{2H} \left(\beta_H(1) - \beta_H \left(\frac{1 + \sin(a + \pi)}{2} \right) + \beta_H \left(\frac{1 + \sin(b)}{2} \right) \right),
\end{aligned}$$

which concludes this case using (25). The last case is similar. $\qquad \square$

$$\square$$

APPENDIX B. PROOFS OF SECTION 2.3

Proof of Proposition 2.4. Note that $X_{\Theta,\Lambda}(0) = X_{H,\alpha_1,\alpha_2}(0) = 0$ a.s. so that $d_{Kol}(X_{\Theta,\Lambda}(0), X_{H,\alpha_1,\alpha_2}(0)) = 0$. Let $x \in \mathbb{R}^2$ with $x \ne 0$. Then, the error of approximation is bounded by

$$\frac{v_{H,\alpha_1,\alpha_2}(x) - v_{\Theta,\Lambda}(x)}{v_{H,\alpha_1,\alpha_2}(x)},$$

with $v_{H,\alpha_1,\alpha_2}(x) = \frac{1}{2}\gamma(H)\|x\|^{2H} \int_{\alpha_1}^{\alpha_2} |\cos(\theta - arg(x))|^{2H} d\theta$ and

$$v_{\Theta,\Lambda}(x) = \frac{1}{2}\gamma(H)\|x\|^{2H} \sum_{i=1}^n \lambda_i |\cos(\theta_i - arg(x))|^{2H}.$$

First let us remark that since $\theta' \mapsto |\cos(\theta - \theta')|^{2H}$ is continuous, non negative and non identically equal to 0 one can find $c_1 > 0$ such that for all $x \in \mathbb{R}^2$, $\int_{\alpha_1}^{\alpha_2} |\cos(\theta - arg(x))|^{2H} d\theta \geq c_1$. It follows that

$$d_{Kol}(X_{\Theta,\Lambda}(x), X_{H,\alpha_1,\alpha_2}(x)) \leq c_1^{-1} \left(\int_{\alpha_1}^{\alpha_2} |\cos(\theta - arg(x))|^{2H} d\theta - \sum_{i=1}^{n} \lambda_i |\cos(\theta_i - arg(x))|^{2H} \right).$$

Now, let us write

$$(26) \qquad g_x(\theta) = |\cos(\theta - arg(x))|^{2H},$$

and remark that

$$(27) \qquad |g_x(\theta) - g_x(\theta')| \leq 2|\theta - \theta'|^{\min(2H,1)} \text{ for all } \theta, \theta' \in \mathbb{R},$$

using the fact that $||t|^{2H} - |t'|^{2H}| \leq 2|t - t'|^{\min(2H,1)}$ for all $t, t' \in [-1,1]$. It follows that there exists $c_2 > 0$ such that for $0 \leq i \leq n$,

$$(28) \qquad \left| \int_{\theta_i}^{\theta_{i+1}} (g_x(\theta) - g_x(\theta_i)) \, d\theta \right| \leq c_2 (\theta_{i+1} - \theta_i)^{1+\min(1,2H)}.$$

Then, choosing $\lambda_1 = \theta_2 - \theta_0$ and $\lambda_i = \theta_{i+1} - \theta_i$ for $2 \leq i \leq n$, one has

$$\left| \int_{\alpha_1}^{\alpha_2} g_x(\theta) - \sum_{i=1}^{n} \lambda_i g_x(\theta_i) \right| \leq c_2 (\alpha_2 - \alpha_1) \max_{0 \leq i \leq n} (\theta_{i+1} - \theta_i)^{\min(1,2H)}.$$

Moreover g_x is of class $\mathcal{C}^2$ on $\mathbb{R} \setminus \{arg(x) - \pi/2 + \pi\mathbb{Z}\}$ with

$$(29) \qquad |g_x''(\theta)| \leq c_3 |\cos(\theta - arg(x))|^{2H-2}, \text{ for all } \theta \notin arg(x) - \pi/2 + \pi\mathbb{Z},$$

for some $c_3 > 0$ (non depending on x). According to the trapezoidal rule, when $[\theta_i, \theta_{i+1}] \cap \{arg(x) - \pi/2 + \pi\mathbb{Z}\} = \emptyset$,

$$(30) \qquad \left| \int_{\theta_i}^{\theta_{i+1}} \left(g_x(\theta) - \frac{g_x(\theta_i) + g_x(\theta_{i+1})}{2} \right) d\theta \right| \leq \sup_{\theta \in [\theta_i, \theta_{i+1}]} |g_x''(\theta)| \frac{(\theta_{i+1} - \theta_i)^3}{12}.$$

Note also that using (27) one always has

$$(31) \qquad \left| \int_{\theta_i}^{\theta_{i+1}} \left(g_x(\theta) - \frac{g_x(\theta_i) + g_x(\theta_{i+1})}{2} \right) d\theta \right| \leq c_2 (\theta_{i+1} - \theta_i)^{1+\min(1,2H)}.$$

For sake of simplicity let us consider the case where $arg(x) = \pi/2$ such that $-\pi/2 \leq \alpha_1 \leq \theta - arg(x) + \pi/2 \leq \alpha_2 \leq \pi/2$ and

$$| \cos(\theta - arg(x))| \geq \frac{2}{\pi}|\theta - arg(x) + \pi/2| = \frac{2}{\pi}|\theta|.$$

If $\theta_{n+1} \leq 0$ we set $m = n + 1$, if $\theta_0 > 0$ we set $m = 0$ and otherwise we choose $m \in \{0, \ldots, n\}$ such that $\theta_m \leq 0 < \theta_{m+1}$. Then, according to (29), since $2H - 2 < 0$, for $i > m + 2$,

$$\sup_{\theta \in [\theta_i, \theta_{i+1}]} |g_x''(\theta)| \leq c_3 \left(\frac{2}{\pi}\right)^{2H-2} \theta_i^{2H-2} \leq c_3 \left(\frac{2}{\pi}\right)^{2H-2} \frac{1}{\theta_{i-1} - \theta_i} \int_{\theta_{i-1}}^{\theta_i} \theta^{2H-2} d\theta,$$

with, when $m < n - 3$,

(32)
$$\sum_{i=m+3}^{n-1} \int_{\theta_{i-1}}^{\theta_i} \theta^{2H-2} d\theta = \int_{\theta_{m+2}}^{\theta_n} \theta^{2H-2} d\theta \leq c_4 \begin{cases} (\theta_{m+2} - \theta_{m+1})^{-1+\min(2H,1)} & \text{if } H \neq 1/2 \\ |\log(\theta_{m+2} - \theta_{m+1})| & \text{if } H = 1/2 \end{cases},$$

for some constants $c_3, c_4 > 0$. While for $i < m - 1$ one has

$$\sup_{\theta \in [\theta_i, \theta_{i+1}]} |g_x''(\theta)| \leq c_3 \left(\frac{2}{\pi}\right)^{2H-2} \frac{1}{\theta_{i+2} - \theta_{i+1}} \int_{\theta_{i+1}}^{\theta_{i+2}} |\theta|^{2H-2} d\theta,$$

with, when $m > 3$,

(33)
$$\sum_{i=1}^{m-2} \int_{\theta_{i-1}}^{\theta_i} \theta^{2H-2} d\theta = \int_{\theta_0}^{\theta_{m-2}} \theta^{2H-2} d\theta \leq c_5 \begin{cases} (\theta_{m-1} - \theta_{m-2})^{-1+\min(2H,1)} & \text{if } H \neq 1/2 \\ |\log((\theta_{m-1} - \theta_{m-2}))| & \text{if } H = 1/2 \end{cases},$$

for some constant $c_5 > 0$. Let us choose $\lambda_1 = (\theta_1 - \theta_0) + \frac{\theta_2 - \theta_1}{2}$, $\lambda_n = (\theta_{n+1} - \theta_n) + \frac{\theta_n - \theta_{n-1}}{2}$ and $\lambda_i = \frac{\theta_{i+1} - \theta_{i-1}}{2}$ for $2 \leq i \leq n - 1$. Then, let us remark that for $2 \leq i \leq n - 1$ one has $\lambda_i = \frac{\theta_{i+1} - \theta_i}{2} + \frac{\theta_i - \theta_{i-1}}{2}$. Therefore

$$\sum_{i=2}^{n-1} \lambda_i g_x(\theta_i) = \sum_{i=2}^{n-1} \frac{\theta_{i+1} - \theta_i}{2} g_x(\theta_i) + \sum_{i=1}^{n-2} \frac{\theta_{i+1} - \theta_i}{2} g_x(\theta_{i+1})$$

$$= \sum_{i=2}^{n-2} (\theta_{i+1} - \theta_i) \frac{g_x(\theta_i) + g_x(\theta_{i+1})}{2} + \frac{\theta_n - \theta_{n-1}}{2} g_x(\theta_{n-1}) + \frac{\theta_2 - \theta_1}{2} g_x(\theta_2).$$

It follows that

$$\sum_{i=1}^{n} \lambda_i g_x(\theta_i) = \sum_{i=1}^{n-1} (\theta_{i+1} - \theta_i) \frac{g_x(\theta_i) + g_x(\theta_{i+1})}{2} + (\theta_1 - \theta_0) g_x(\theta_1) + (\theta_{n+1} - \theta_n) g_x(\theta_n)$$

$$= \sum_{i=1}^{n-1} \int_{\theta_i}^{\theta_{i+1}} \frac{g_x(\theta_i) + g_x(\theta_{i+1})}{2} d\theta + \int_{\theta_0}^{\theta_1} g_x(\theta_1) d\theta + \int_{\theta_n}^{\theta_{n+1}} g_x(\theta_n) d\theta.$$

Then,

$$\left| \int_{\alpha_1}^{\alpha_2} g_x(\theta) - \sum_{i=1}^{n} \lambda_i g_x(\theta_i) \right|$$

$$\leq \sum_{i=1}^{n-1} \left| \int_{\theta_i}^{\theta_{i+1}} g_x(\theta) - \frac{g_x(\theta_i) + g_x(\theta_{i+1})}{2} d\theta \right| + \left| \int_{\theta_0}^{\theta_1} g_x(\theta) - g_x(\theta_1) d\theta \right| + \left| \int_{\theta_n}^{\theta_{n+1}} g_x(\theta) - g_x(\theta_n) d\theta \right|$$

$$\leq \sum_{i=1}^{m-2} + \sum_{i=m+3}^{n-1} + \sum_{i=m-1}^{m+2} + \left| \int_{\theta_0}^{\theta_1} g_x(\theta) - g_x(\theta_1) d\theta \right| + \left| \int_{\theta_n}^{\theta_{n+1}} g_x(\theta) - g_x(\theta_n) d\theta \right|,$$

which gives the result using (30) with (32) and (33) for the two first sums and using (28) and (31) for the other terms. The general case where $arg(x) \neq \pi/2$ can be computed similarly. $\qquad\square$

Proof of Proposition 2.5. The proof is similar to the proof of Proposition 2.4, considering

$$\tilde{g}_x(\theta) = \gamma(h(\theta)) c(\theta) |x \cdot u(\theta)|^{2h(\theta)} = \gamma(h(\theta)) c(\theta) \|x\|^{2h(\theta)} |\cos(\theta - arg(x))|^{2h(\theta)}.$$

instead of $g_x(\theta)$ given by (26). Note that when h and c are assumed of class $\mathcal{C}^l$ ($l = 1$ or 2) on $[\alpha_1, \alpha_2] \subset [-\pi/2, \pi/2]$, one can find $C > 0$ such that for all $x \in T$,

$$|\tilde{g}_x(\theta) - \tilde{g}_x(\theta')| \leq C |\theta - \theta'|^{\min(2H(\alpha_1, \alpha_2), 1)}, \text{ for all } \theta, \theta' \in [\alpha_1, \alpha_2],$$

and when $l = 2$,

$$|\tilde{g}_x''(\theta)| \leq C |\cos(\theta - arg(x))|^{2H(\alpha_1, \alpha_2) - 2}, \text{ for all } \theta \in [\alpha_1, \alpha_2] \text{ with } \theta \notin arg(x) - \pi/2 + \pi\mathbb{Z},$$

where $H(\alpha_1, \alpha_2) = \min_{\theta \in [\alpha_1, \alpha_2]} h(\theta)$. These estimates allow to proceed as in the proof of Proposition 2.4. The result follows by summing the integrals over which the functions h and c are regular using the fact that $H \leq H(\alpha_1, \alpha_2)$ for all α_1, α_2. $\qquad\square$

Appendix C. Optimal band selection

input : α_1, α_2, defining the considered angular interval

ε: the maximum angular distance between two adjacent bands

r: resolution parameter (the sampling step is $1/r$)

output: a finite sequence of integer vectors $(\bar{p}_k, \bar{q}_k)_{1 \leq k \leq s}$

1     $N \leftarrow 1 + \lceil \frac{1}{\tan \varepsilon} \rceil$

2   Build the set $\mathcal{V}$ of all integer vectors $(q, p) \in \{1, \ldots, N\} \times \{-N, \ldots, N\}$ such that $\gcd(p, q) = 1$ and $\alpha_1 < \angle(q, p) < \alpha_2$

3   Sort $\mathcal{V}$ into a sequence $(p_k, q_k)_{1 \leq k \leq n}$ with $k \mapsto \theta_k := \angle(q_k, k_k)$ increasing

4   Compute the angle $\theta_k := \angle(q_k, p_k)$ and the cost e_k associated to each (q_k, p_k)

5   Add extremal angles: $\theta_0 \leftarrow \alpha_1$ ($e_0 \leftarrow 0$) and $\theta_{n+1} \leftarrow \alpha_2$

6     $c_{n+1} \leftarrow 0$

7   **for** $i = n, n-1, \ldots 0$ **do**

8         $cmin \leftarrow \infty$

9         $j \leftarrow i + 1$

10   **while** $j \leq n+1$ *and* $\theta_j \leq \theta_i + \varepsilon$ **do**

11   **if** $c_j \leq cmin$ **then**

12               $cmin \leftarrow c_j$

13               $k_i \leftarrow j$

14   **end**

15            $j \leftarrow j + 1$

16   **end**

17        $c_i \leftarrow e_i + cmin$

18   **end**

19     $i \leftarrow 0$

20     $s \leftarrow 1$

21   **while** $i \leq n$ **do**

22         $i \leftarrow k_i$

23         $(\bar{p}_s, \bar{q}_s) \leftarrow (p_i, q_i)$

24         $s \leftarrow s + 1$

25   **end**

26   `return` $(\bar{p}_k, \bar{q}_k)_{1 \leq k \leq s}$

Acknowledgements

References

[1] A. Averbuch, R. Coifman, D. Donoho, M. Israeli, and Y. Shkolnisky. A framework for discrete integral transformations I - the pseudo-polar Fourier transform. *SIAM Journal on Scientific Computing*, 30(2):764–784, 2008.

[2] A. Averbuch, R. Coifman, D. Donoho, M. Israeli, and Y. Shkolnisky. A framework for discrete integral transformations II - the 2D discrete Radon transform. *SIAM Journal on Scientific Computing*, 30(2):785–803, 2008.

[3] A. Ayache, A. Bonami, and A. Estrade. Identification and series decomposition of anisotropic Gaussian fields, 2005. *Proceedings of the Catania ISAAC'05 congress.*

[4] R. Bellman. The theory of dynamic programming. *Bull. Amer. Math. Soc.*, 60:503–515, 1954.

[5] H. Biermé, C.L. Benhamou, and F. Richard. Parametric estimation for gaussian operator scaling random fie lds and anisotropy analysis of bone radiograph textures. In K. Pohl, editor, *Proc. of the International Conference on Medical Image Computing and Computer Assisted Intervention (MICCAI'09), Workshop on Probabilistic Model s for Medical Imaging*, pages 13–24, London, UK, september 2009.

[6] H. Biermé, A. Bonami, and León J. R. Central limit theorems and quadratic variations in terms of spectral density. *Electronic Journal of Probability*, 16(3):362–395, 2011.

[7] H. Biermé and F. Richard. Estimation of anisotropic gaussian fields through Radon transform. *ESAIM:P& S*, 12(1):30–50, 2008.

[8] H. Biermé and F. Richard. *ESAIM Proceedings: Mathematical Methods for Imaging and Inverse Problems*, volume 26, chapter Anisotropic texture modeling and applications to medical image analysis, pages 100–122. Springer, H. Ammari edition, 2009.

[9] A. Bonami and A. Estrade. Anisotropic analysis of some Gaussian models. *J. Fourier Anal. Appl.*, 9(3):215–236, 2003.

[10] P. Brooker. Two-dimensional simulation by turning bands. *Mathematical Geology*, 17(1):81–90, 1985.

[11] A. Brouste, S. Lambert-Lacroix, and Istas J. On fractional gaussian random fields simulations. *Journal of Statistical Software*, 23(1):1–23, 2007.

[12] G. Chan. An effective method for simulating Gaussian random fields. In *Proceedings of the statistical Computing section*, pages 133–138, `www.stat.uiowa.edu/~grchan/`, 1999. Amerir. Statist.

[13] J. Chilès and P. Delfiner. *Geostatistics: modeling spatial uncertainty*. Wiley, New-York, 1999.

[14] J.P. Chilès. *Géostatique des phénomènes non stationnaires*. PhD thesis, Université de Nancy, 1977.

[15] G. Christakos. Stochastic simulation of spatially correlated geo-processes. *Mathematical Geology*, 19(8):807–831, 1987.

[16] S. Davies and P. Hall. Fractal analysis of surface roughness by using spatial data. *Journal of the Royal Statistical Society, Series B*, 61:3–37, Fractal analysis of surface roughness by using spatial data.

[17] C. Dietrich. A simple and efficient space domain implementation of the turning bands method. *Water Resources Research*, 31(1):147–156, 1995.

[18] C.R. Dietrich and G.N. Newsam. Fast and exact simulation of stationary gaussian processes through circulant embedding of the covariance matrix. *SIAM Journal of Scientific Computing*, 18(4):1088–1107, 1997.

[19] R. Dimitrakopoulos. Conditional simulation of intrinsic random functions of order k. *Mathematical Geology*, 22(3):361–380, 1990.

[20] X. Emery. A turning bands program for conditional co-simulation of cross-correlated Gaussian random fields. *Computer and Geosciences*, 34(12):1850–1662, 2008.

[21] X. Emery and C. Lantuéjoul. TBSIM: A computer program for conditional simulation of three-dimensional Gaussian random fields via the turning bands method. *Computer and Geosciences*, 32(10):1615–1628, 2006.

[22] X. Emery and C. Lantuéjoul. A spectral approach to simulating intrinsic random fields with power and spline generalized covariances. *Computer and Geosciences*, 12(1):121–132, 2008.

[23] T. Gneiting. Comment on "a simple and efficient space domain implementation of the turning bands method" by C. Dietrich. *Water Resources Research*, 32(11):3391–3396, 1996.

[24] T. Gneiting. Closed form solutions of the two-dimensional turning bands equation. *Mathematical Geology*, 30(4):379–390, 1998.

[25] A. Journel. Geostatistics for conditional simulation of ore bodies. *Economic Geology*, 69(5):673–687, 1974.

[26] A. N. Kolmogorov. Wienersche Spiralen und einige andere interessante Kurven in Hilbertsche Raum. *C. R. (Dokl.) Acad. Sci. URSS*, 26:115–118, 1940.

[27] C. Lacaux. *Real Harmonizable multifractional Levy field*. PhD thesis, Université de Toulouse, 2004.

[28] C. Lantuéjoul. *Geostatistical Simulation: Models and Algorithms*. Springer, 2002.

[29] B. B. Mandelbrot and J. Van Ness. Fractional Brownian motion, fractionnal noises and applications. *SIAM Review*, 10:422–437, 1968.

[30] A. Mantoglou. Digital simulation of multivariate two- and three-dimensional stochastic processes with a spectral turning bands method. *Mathematical Geology*, 19(2):129–149, 1987.

[31] A. Mantoglou and J. Wilson. The turning bands method for simulation of random fields using line generation by a spectral method. *Water Resources Research*, 18(5):1379–1394, 1982.

[32] G. Matheron. The intrinsic random functions and their application. *Adv. Appl. Prob.*, 5:439–468, 1973.

[33] E. Pardo-Igúzquiza and M. Chica-Olmo. The Fourier integral method: an efficient spectral method for simulation of random fields. *Mathematical Geology*, 25(2):177–217, 1993.

[34] E. Pardo-Igúzquiza and P. Dowd. IRFK2D: a computer program for simulating intrinsic random functions of order k. *Computers and Geosciences*, 29(6):753–759, 2003.

[35] E. Perrin, R. Harba, R. Jennane, and I. Iribarren. Fast and exact synthesis for 1-D fractional Brownian motion a nd fractional gaussian noises. *IEEE Signal Processing Letters*, 9(11):382–384, 2002.

[36] F. J.P. Richard and H. Biermé. Statistical tests of anisotropy for fractional Brownian textures. application to full-field digital mammography. *Journal of Mathematical Imaging and Vision*, 36(3):227–240, 2010.

[37] G. Samorodnitsky and M. S. Taqqu. *Stable non-Gaussian random processes*. Stochastic Modeling. Chapman & Hall, New York, 1994. Stochastic models with infinite variance.

[38] D. Saupe. *The science of fractal images*, chapter Algorithms for random fractals. Springer-Verlag, New-York, H.-O. Peitgen and D. Saupe edition, 1988.

[39] M. Setas and J. Rebordao. Modeling anisotropic and fractal two-dimensional fields: a tool for image simulation. *Optical Engineering*, 39(6):1497–1506, 2000.

[40] M. Shinozuka and C.-M. Jan. Digital simulation of random processes and its applications. *Journal of Sound and Vibration*, 25(1):111 − 128, 1972.

[41] M. L. Stein. Fast and exact simulation of fractional Brownian surfaces. *Journal of Computational and Graphical Statistics*, 11(3):587–599, 2002.

[42] A. Wood and G. Chan. Simulation of stationary Gaussian proceses on $[0,1]^d$. *Journal of Computational and Graphical Statistics*, 3(4):409–432, 1994.

[43] J. Wu. Analyses and simulation of anisotropic fractal surfaces. *Chaos, Solitons and Fractals*, 13(9):1791–1806, 2002.

[44] Yimin Xiao. Sample path properties of anisotropic Gaussian random fields. In *A minicourse on stochastic partial differential equations*, volume 1962 of *Lecture Notes in Math.*, pages 145–212. Springer, Berlin, 2009.

[45] Z. Yin. New methods for simulation of fractional Brownian motion. *Journal of Computational Physics*, 127(1):66–72, 1996.

[1] MAP5, UMR-CNRS 8145, Université Paris Descartes, PRES Sorbonne Paris Cité, 45 rue des Saints-Pères, 75006 Paris, France.

E-mail address: [bierme,moisan]@mi.parisdescartes.fr

[2] LMPT, UMR-CNRS 7350, Fédération Denis Poisson FR-CNRS 2964, Université François-Rabelais de Tours, Parc de Grandmont, 37200 Tours, France.

[3] LATP, UMR-CNRS 7353, Aix-Marseille Université, 39 rue F. Joliot Curie, 13453 Marseille Cedex 13, France.

E-mail address: frederic.richard@univ-amu.fr